The Meteoritical Society

Meteoritics & Planetary Science 50, Nr 12, 2099–2120 (2015)
doi: 10.1111/maps.12565

Nickeliferous pyrite tracks pervasive hydrothermal alteration in Martian regolith breccia: A study in NWA 7533

Jean-Pierre LORAND[1*], Roger H. HEWINS[2,3], Laurent REMUSAT[2], Brigitte ZANDA[2,3,4], Sylvain PONT[2], Hugues LEROUX[5], Maya MARINOVA[6], Damien JACOB[5], Munir HUMAYUN[7], Alexander NEMCHIN[8], Marion GRANGE[8], Allen KENNEDY[8], and Christa GÖPEL[9]

[1]Laboratoire de Planétologie et Géodynamique à Nantes, CNRS UMR 6112, Université de Nantes, 2 Rue de la Houssinère, BP 92208, 44322 Nantes Cédex 3, France
[2]Institut de Minéralogie, de Physique des Matériaux et de Cosmochimie (IMPMC)—Sorbonne Université- Muséum National d'Histoire Naturelle, UPMC Université Paris 06, UMR CNRS 7590, IRD UMR 206, 61 rue Buffon, 75005 Paris, France
[3]Department of Earth & Planetary Sciences, Rutgers University, Piscataway, New Jersey 08854, USA
[4]Institut de Mécanique Céleste et de Calcul des Ephémérides—Observatoire de Paris—CNRS UMR 8028, 77 av. Denfert-Rochereau, 75014 Paris, France
[5]Unité Matériaux et Transformations, Université Lille 1 & CNRS, UMR 8207, 59655 Villeneuve d'Ascq, France
[6]Institut Michel-Eugène Chevreul, Université Lille 1 & CNRS, FR 2638, 59655 Villeneuve d'Ascq, France
[7]Department of Earth Ocean & Atmospheric Science and National High Magnetic Field Laboratory, Florida State University, Tallahassee, Florida 32310, USA
[8]Department of Applied Geology, Curtin University, Perth, Western Australia 6845, Australia
[9]Institut de Physique du Globe Sorbonne Paris Cité, University Paris Diderot,CNRS UMR 7154, F-75005 Paris, France
[*]Corresponding author. E-mail: jean-pierre.lorand@univ-nantes.fr

(Received 02 February 2015; revision accepted 16 September 2015)

Abstract–Martian regolith breccia NWA 7533 (and the seven paired samples) is unique among Martian meteorites in showing accessory pyrite (up to 1% by weight). Pyrite is a late mineral, crystallized after the final assembly of the breccia. It is present in all of the lithologies, i.e., the fine-grained matrix (ICM), clast-laden impact melt rocks (CLIMR), melt spherules, microbasalts, lithic clasts, and mineral clasts, all lacking magmatic sulfides due to degassing. Pyrite crystals show combinations of cubes, truncated cubes, and octahedra. Polycrystalline clusters can reach 200 μm in maximum dimensions. Regardless of their shape, pyrite crystals display evidence of very weak shock metamorphism such as planar features, fracture networks, and disruption into subgrains. The late fracture systems acted as preferential pathways for partial replacement of pyrite by iron oxyhydroxides interpreted as resulting from hot desert terrestrial alteration. The distribution and shape of pyrite crystals argue for growth at moderate to low growth rate from just-saturated near neutral ($6 < pH < 10$), H_2S-HS-rich fluids at minimum log fO_2 of >FMQ + 2 log units. It is inferred from the maximum Ni contents (4.5 wt%) that pyrite started crystallizing at 400–500 °C, during or shortly after a short-duration, relatively low temperature, thermal event that lithified and sintered the regolith breccias, 1.4 Ga ago as deduced from disturbance in several isotope systematics.

INTRODUCTION

The sulfur cycle is one of the most important geochemical cycles on Mars (King and McLennan 2010; Franz et al. 2014). Oxidized sulfur is a major component of the Martian regolith, with SO_3 concentrations up to 8% (King and McLennan [2010] and references therein). Odyssey gamma-ray spectrometer (GRS) integrated observations suggest a Mars global average surface sulfur abundance of 4.40 wt% SO_3, reflecting a mixture of soils with higher sulfur abundances and bedrock with lower average sulfur abundances (Dyar et al. 2011). Oxidized

sulfur in Mars modern soils is combined with metallic cations (namely Fe, Ca, Mg, Al), as water-soluble sulfates. The origin of these sulfates is still under discussion. They were considered to be evaporitic precipitates, acid fog alteration of basalts or basaltic ashes, alteration of impact debris or supergene alteration of magmatic sulfides inside basalt bedrocks (Klingelhöffer et al. 2004; Tosca et al. 2004; Gendrin et al. 2005; McCollom and Hynek 2005; Knauth et al. 2005; see King and McLennan [2010] and references therein). The hypothesis of sulfide alteration by H_2O–O_2 has gained popularity because it is able to generate both highly acidic conditions suitable for decomposition of silicates liberating sulfate-forming cations (Fe, K, Ca, Mg) and oxidative conditions stabilizing iron oxyhydroxides ultimately producing hematite spherules by dehydration, as in the Burns formation (Chevrier et al. 2004; Dehouck et al. 2012).

There remain considerable uncertainties regarding Martian bedrock sulfide mineralogy which markedly depends on local redox conditions and rock lithologies. Theoretical electrochemical models (e.g., Burns and Fisher 1990) and alteration experiments (e.g., Chevrier et al. 2004, 2006; Dehouck et al. 2012) assumed sulfur-deficient sulfides (pyrrhotite) to be stable sulfides. Studies of Martian (SNC) meteorites reported pyrrhotite as the predominant Fe-sulfide (Rochette et al. 2001; Lorand et al. 2005, 2012; Chevrier et al. 2011; Gattacceca et al. 2013; Franz et al. 2014) in agreement with the fO_2 conditions inferred for the Martian mantle (QFM+0.5 to QFM−3; Herd et al. 2002; Papike et al. 2009). A basic prerequisite of models assuming alteration of magmatic sulfides is preconcentration of sulfides at levels much higher than usually reported in Martian basalts (<3000 ppm S) to account for the global amount of sulfates on Mars (e.g., Burns and Fisher 1990; Dehouck et al. 2012). To date no evidence of magmatic sulfide ore bodies has been reported on Mars, neither by remote sensing orbiter data nor by rovers. It is well known that shock melts are strongly degassed (very low water, CO_2, and S contents), so the heavily cratered southern highlands terrains are expected to be ultradepleted with respect to magmatic sulfur. Troilite (FeS) being easily melted and vaporized (e.g., Yamaguchi et al. 1999), even low-T impactites may have lost S, as shown by strongly shocked chassignite NWA 2737 (Lorand et al. 2012).

Zolotov and Shock (2005) by-passed the problem for the Burns formation at the landing site of the rover Opportunity by assuming that hydrothermal processes preconcentrated sulfur as pyrite deposits in a depression. Fe-disulfides (pyrite/marcasite) have been reported to replace the pyrrhotite in some veins inside nakhlites/chassignites (Floran et al. 1978; Greenwood et al. 2000; Franz et al. 2014), likely connected to oxidation by Fe^{3+} sulfate precipitation in the same rock (Bridges et al. [2001] and references therein). Micrometer-sized pyrite grains replacing pyrrhotite were reported in ALH 84001 as shock products (Shearer et al. 1996; Scott 1999; Greenwood et al. 2000). Vaniman et al. (2013) pointed out the occurrence of both pyrrhotite (1 ± 0.5 wt%) and pyrite in Yellowknife mudstone deposits of the late Noachian/early Hesperian Gale crater, analyzed by Curiosity. All these occurrences provide evidence for reduced sulfur of different origins close to the Martian surface.

Unlike other Martian meteorites, NWA 7533, like NWA 7034 (Agee et al. 2013) and the six other paired samples (NWA 7455, NWA 7906, NWA 7907, NWA 8114, NWA 8171, NWA 8674) have been identified as polymict breccias likely coming from the surface of Mars (Humayun et al. 2013; Wittmann et al. 2015). These meteorites contain fine-grained clasts that chemically resemble Martian soils of the Gusev crater. NWA 7533 was interpreted as an impact breccia containing pieces of Pre-Noachian terrains of Mars (zircon in monzonitic clasts with U-Pb crystallization age of 4423 ± 26 Myr) and disseminated chondritic impactor material amounting up to 5% by weight according to the highly siderophile element contents measured by LA-ICPMS (Humayun et al. 2013; Hewins et al. 2014a). For NWA 7455, the mean Ir concentrations correspond to a component of 3.1% CI chondrite (Wittmann et al. 2015). Impact breccias are also unique among Martian meteorites in showing widespread crystallization of large (up to 150 μm) euhedral pyrite crystals (Lorand et al. 2014). These authors detected Ni-rich crystals (up to 4.5 wt% Ni), while Wittmann et al. (2015) in NWA 7455 identified Ni-poor pyrite crystals that preceded the formation of Ca-carbonate-filled veins in a small melt spherule as well as euhedral pyrite crystals that are partly altered to (possibly) goethite in vitrophyric clasts and in recrystallized feldspathic clasts. NWA 7533 promises to shed new light on possible links between this sulfide precipitation, impact events, and hydrothermal alteration of the Martian crust. Our aim was to characterize this event from a detailed study of textural and compositional features of pyrite and to place it in the chronology of events recorded by NWA 7533.

PETROGRAPHIC DATA

NWA 7533 consists of a fine-grained interclast matrix (acronym ICM) containing lithic clasts of microbasalts, norite, monzonite, and single minerals derived from these rocks (plagioclase, perthitic alkali feldspar, orthopyroxene, inverted pigeonite, augite,

chromite, and Fe-Ti oxides), as well as clast-laden impact melt rocks (CLIMR) and melt spherules (Fig. 1). Like NWA 7455, NWA7533 shows occasional calcitized networks sealing pre-existing fracture planes and discontinuities throughout the meteorite.

Geochemically, the spherules, the groundmass of the melt rock, and the microbasalts resemble melted windblown dust and regolith debris (Humayun et al. 2013). The chemical composition of the fine-grained material in both the clasts and in the interclast matrix is very similar and was modeled as derived from crystallization products from a low-degree partial melt (<5%) of a chondritic garnet peridotite source (Humayun et al. 2013). Some zircons bear the imprint of a shock event at 1712 ± 85 Myr (Nemchin et al. 2014) and apatite Pb-Pb closure ages are about 1.4 Ga (Bellucci et al. 2015).

Clast-laden impact melt rocks (CLIMR) are dominated by plagioclase laths and subophitic pyroxene. An unusual characteristic of the clast-laden melt rocks is the presence of oval or polygonal clots of very finely granular to radiating fibrous pyroxene surrounded by aureoles of plagioclase needles radiating outward from the clots. Fine-grained basalt clasts (Hewins et al. 2013) with subophitic to granoblastic textures, grain size ~20–100 μm, are composed of orthopyroxene $En_{73–63}$ or pigeonite $En_{63–49}$, augite $En_{46–29}$, plagioclase $An_{66–30}$, and Fe-rich spinel. Their bulk compositions are close to those of the clast-laden impact melt rocks and contain high levels of siderophile elements (Humayun et al. 2013). They are interpreted as impact melt that crystallized less rapidly than CLIMR, which were quenched more rapidly due to incorporation of abundant clasts.

Petrologically, the dense nanocrystalline matrix containing the clasts looks like annealed windblown dust with a granoblastic texture (Hewins et al. 2013; Muttik et al. 2014a, 2014b). It is similar mineralogically to CLIMR and contains crystal clasts down to ~5 μm. It consists of anhedral micrometer-sized plagioclase with submicrometer-sized pyroxene surrounding and embedded in it, plus fine-grained Fe-(Ti) oxides—magnetite, often symplectitic or lacy and maghemite, identified by XRD (Pont, unpublished data). A similar mineral assemblage was previously reported in NWA 7034 matrix by Agee et al. (2013) and Gattacceca et al. (2014).

Crystal clasts are fragments of disaggregated lithic clasts including pyroxenes, feldspars, Fe-Ti oxides, chlorapatite, and accessory minerals (notably zircon and baddeleyite). Pyroxenes are either deep-seated clasts containing exsolution, or zoned pyroxene of near surface origin. The most magnesian orthopyroxene ($En_{80–73}$) is never attached to plagioclase, though

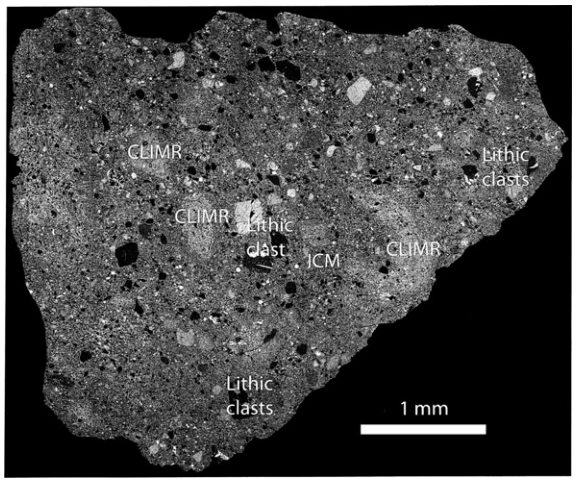

Fig. 1. Low-magnification BSE image of part of NWA 7533-1 (after Humayun et al. 2013). CLIMR = clast-laden impact melt rock; ICM = interclast matrix. Very dark gray are feldspar clasts; medium gray, pyroxene clasts; off white, apatite, Fe oxides, and oxihydroxides.

associated with chrome spinel and rarely augite. It most likely derives from pyroxenites, perhaps pristine crustal rocks of the early Martian crust as suggested by its very low Ni concentrations (Hewins et al. 2014a). More ferroan pyroxene ($En_{<72}$), orthopyroxene, or inverted pigeonite, is often attached to plagioclase and much of it must come from noritic rocks. Plagioclase $An_{50–30}$ is widely distributed in different lithic clast types. Alkali feldspar, often perthitic, is associated with plagioclase (An<30), ferroan pyroxene, chlorapatite, and magnetite + ilmenite + accessory rutile in monzonitic clasts. Zircon and baddeleyite are found in these highly fractionated rocks, and also as individual mineral clasts. Oxygen isotope compositions of zircon indicate prolonged interaction between the Martian regolith with Martian atmosphere and hydrosphere (Nemchin et al. 2014).

Of course, firmly identifying a source region on Mars for regolith breccias is challenging. A connection with the southern highlands which are heavily cratered was inferred by Hewins et al. (2013) and Humayun et al. (2013) from pre-Noachian zircons, highly siderophile element contents, and the polymict nature of breccia including impact melts of various origins and various lithologies. More recently, Beck et al. (2015) showed that the low reflectance and the absence of absorption features in reflectance spectra of NWA 7533 strengthen this connection with the southern highlands which have a low albedo and are mostly devoid of spectral features. Likewise Wittmann et al. (2015) found a reasonable compositional match for the Th and Fe abundance in NWA 7475 in the Terra Sirenum region, at 30°S/165°W.

ANALYTICAL METHODS

Pyrite and its alteration products were first characterized in reflected light using a Zeiss photomicroscope. Five polished sections (labeled NWA 7533-1 to NWA7533-5) and a thin section (Beck et al. 2015) representing altogether a total surface area of ~6 cm^2, were then studied with a Tescan VEGA II LSU scanning electron microscope (SEM) operating in conventional (high-vacuum) mode, and equipped with an SD3 (Bruker) EDS detector (Muséum National d'Histoire Naturelle Paris, France = MNHN). Pyrite crystals were located on low-magnification (×500) backscattered electron maps, which allowed pyrite modal abundances to be estimated using brightness contrast with nonsulfide minerals (Photoshop™ toolbar).

After a careful SEM study of several hundred crystals, one pyrite grain, showing an almost perfect cubic shape and a fracture network containing alteration material, was selected for a transmission electron microscopy (TEM) investigation (Fig. 2A). An electron transparent sample was extracted from a thin section by the focused ion beam (FIB) technique using an FEI Strata DB 235 at IEMN, University of Lille, France. The TEM characterizations were performed using an FEI Tecnai G2-20 Twin (LaB_6, 200 kV) equipped with a precession system (Nanomegas Company) at the electron microscopy center of the University of Lille. The microstructure was studied by conventional bright field imaging. The identification of the crystallographic structures was performed using electron diffraction. A scanning TEM (STEM) probe was used for the acquisition of microanalysis spectra by X-ray energy dispersive spectroscopy (EDS). Microanalysis data were processed taking into account k-factors and absorption corrections.

Pyrite compositions were analyzed with the MNHN SEM on 140 crystals at 15 kV accelerating voltage by a PhiRoZ EDS standardless procedure (350 analyses) after careful imaging of each grain in the BSE mode at high magnification (×2000 to ×10,000) to avoid overlap with silicate microinclusions or alteration products. The spatial resolution of the SEM (a few hundred nanometers) allowed tiny Fe oxyhydroxides contamination to be resolved and detailed investigation of the Ni distribution to be made from 4 to 6 spot analyses per pyrite grain. The accuracy and precision of SEM analyses were checked by replicate analyses of a terrestrial troilite (Del Norte County; California) previously analyzed by both electron microprobe (EMP) and SEM (Chevrier et al. 2011; Lorand et al. 2012). Section 5 pyrites, on average the least altered of NWA 7533 pyrites, were reanalyzed with the Camparis SXFive Cameca electron microprobe, using two different analytical set-ups: one program for major elements at 15 kV accelerating voltage and 20 nA as sample current, and another for a few trace chalcophile elements (Co, Zn, Cu, As, Se) at 20 kV accelerating voltage, 250 nA as sample current, and longer counting times (60 s/peak). Elemental concentrations were determined using the following standards: natural pyrite for S; sphalerite for Zn; and pure metals for Fe, Ni, Co, Cu, As, Se.

To investigate the origin of pyrite alteration products, D/H ratios of Fe oxyhydroxides were analyzed on five pyrite crystals of an epoxy-free thin section by the NanoSIMS installed at MNHN Paris. Samples were C coated (20 nm thick) and in addition an electron-flooding gun was used for charge compensation. A 30 pA Cs^+ primary beam was used to collect H^- and D^- secondary ions in multicollection mode. In order to identify the location of hydrated phases on a fresh surface, a 25 × 25 μm^2 surface area was presputtered, using a 400 pA Cs^+ beam for 30 min, to remove coating and surface contamination and to reach the sputtering steady-state. Then, we imaged a 20 × 20 μm^2 surface area divided into 256 × 256 pixels at a raster speed of 1 ms/pixel. Surface contamination is known to be more severe when rastering large surfaces (Stephant et al. 2014). In order to check for the isotopic composition determined by images covering 400 μm^2, we have measured the D/H ratio on some selected locations using a smaller raster size. To this end, an 8 × 8 μm^2 surface area, divided into 64 × 64 pixels, was rastered at 1 ms/pixel. An electronic gating (beam blanking) was applied to hinder contamination from the sides of the area of interest; only ions from the inner 5.5 × 5.5 μm^2 were accumulated. Immediately prior to each acquisition, the 400 pA Cs^+ beam was applied over 10 × 10 $micrometer^2$ surface area for 2 min to remove any contamination that had redeposited on the surface. The analysis chamber remained around 10^{-9} Torr in the course of the session. Images were processed using the L'image software (Larry Nittler, Carnegie Institution of Washington). Instrumental fractionation was corrected using a terrestrial goethite sample (SEM–EDS analysis) from the mineralogical collection of the National Museum of Natural History in Paris (sample #2009-2475, Betafo, Madagascar). This sample, a pyrite alteration product, was pressed on clean In foil to reduce pollution from epoxy and C coated (20 nm thick).

SULFIDE MINERALOGY

No magmatic sulfide assemblage (i.e., pyrrhotite–pentlandite–chalcopyrite) similar to those reported in

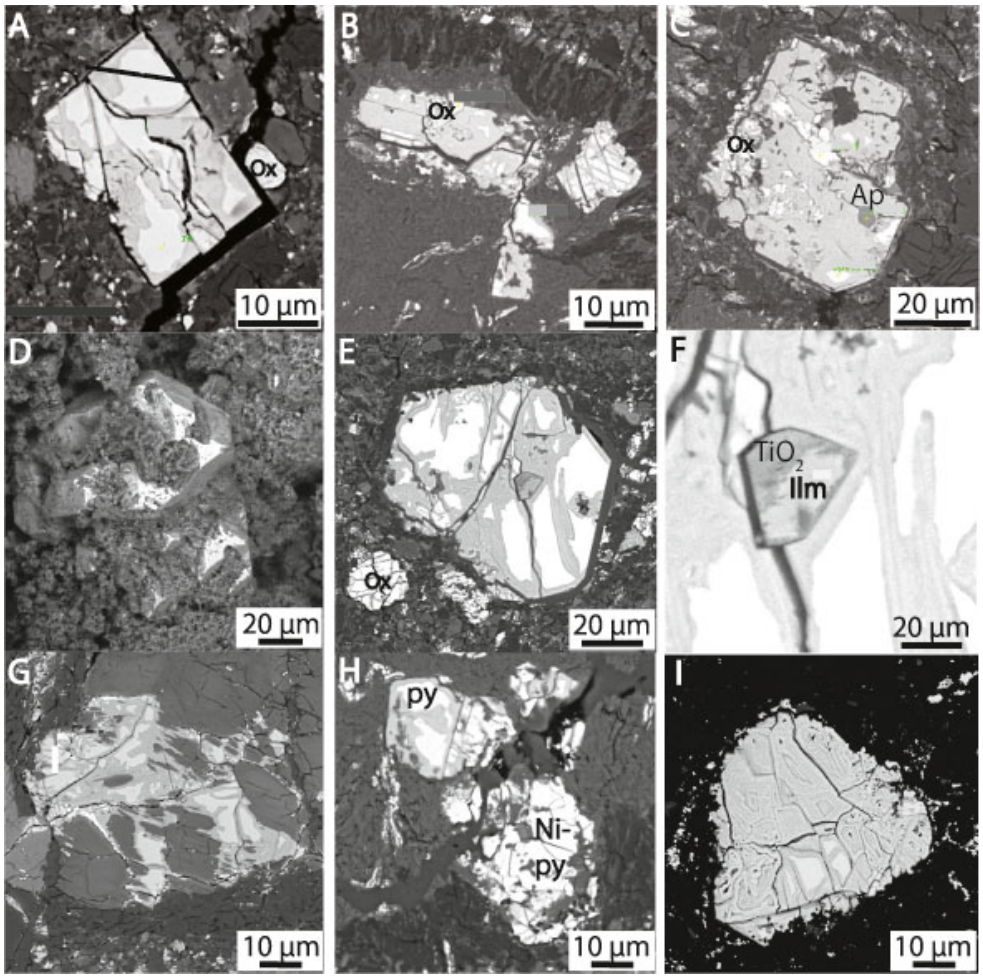

Fig. 2. Backscattered electron (BSE) images of NWA 7533 pyrite crystals. A) Near perfect, slightly altered pyrite cube inside interclast matrix (ICM). Black line indicates the area from which the FIB-TEM sample was extracted. B) Polycrystalline pyrite showing planar deformations in a pyroxene clot; pyrite is attached to Fe (Ti) oxides (ox). C) Strongly altered, poikiloblastic pyrite cube surrounded by a fine-grained dust of ICM minerals; solid inclusions are skeletal Fe (Ti) oxides (ox), Ca pyroxene, plagioclase, and a perfectly euhedral apatite (Ap). D) Open voids with calcitized walls, a few mm deep, providing three-dimensional views of an unusually big cubo-octahedral crystal. E) Octaedral pyrite side-by-side with Fe-Ti oxide micrograins (ox). F) Enlargment of Fig. 2E showing an ilmenite (Ilm) inclusion in pyrite, mantled by micron-thick Fe-depleted rim identified as a TiO_2-rich phase (EDS spectra). G) Low-Ca pyroxene clast partly replaced by pyrite that infiltrates cleavage planes in the pyroxene. Note that the shape of original pyroxene clast was preserved, and both pyrite and low-Ca pyroxene were affected by late fracturing that also guided terrestrial weathering (dark gray). H) Anhedral pyrite grain located in a pyroxene clot and showing a Ni-rich nucleus (Ni-Py). Note the weaker alteration degree of the Ni-rich pyrite compared to the low-Ni pyrite. I) Octaedral pyrite crystals totally replaced by zoned Fe oxyhydroxides (dark gray): note well-preserved concentric microtextures inside the alteration products.

SNC meteorites (Lorand et al. 2005; Franz et al. 2014) was observed in any lithic clasts. Pyrrhotite was identified in only three plagioclase clasts. One, 18 × 10 µm, is made from Ni-bearing pyrrhotite (3 wt% Ni) + pentlandite; it is preserved in a plagioclase/perthitic orthoclase clast, side-by-side with euhedral apatite inclusions. Such sulfide assemblages are very similar to those reported in picritic shergottites (Gattacceca et al. 2013).

Pyrite was first identified because of its lack of anisotropism in crossed-polarized reflected light microscopy. It is widespread and distributed quite uniformly throughout the six sections of NWA 7533 investigated here (Fig. 3). Partial replacement of pyrite by Fe oxyhydroxides makes quantitative modal estimates difficult (Fig. 2). Image analyses on low-magnification BSE maps taking into account both unaltered pyrite and oxyhydroxide pseudomorphs that

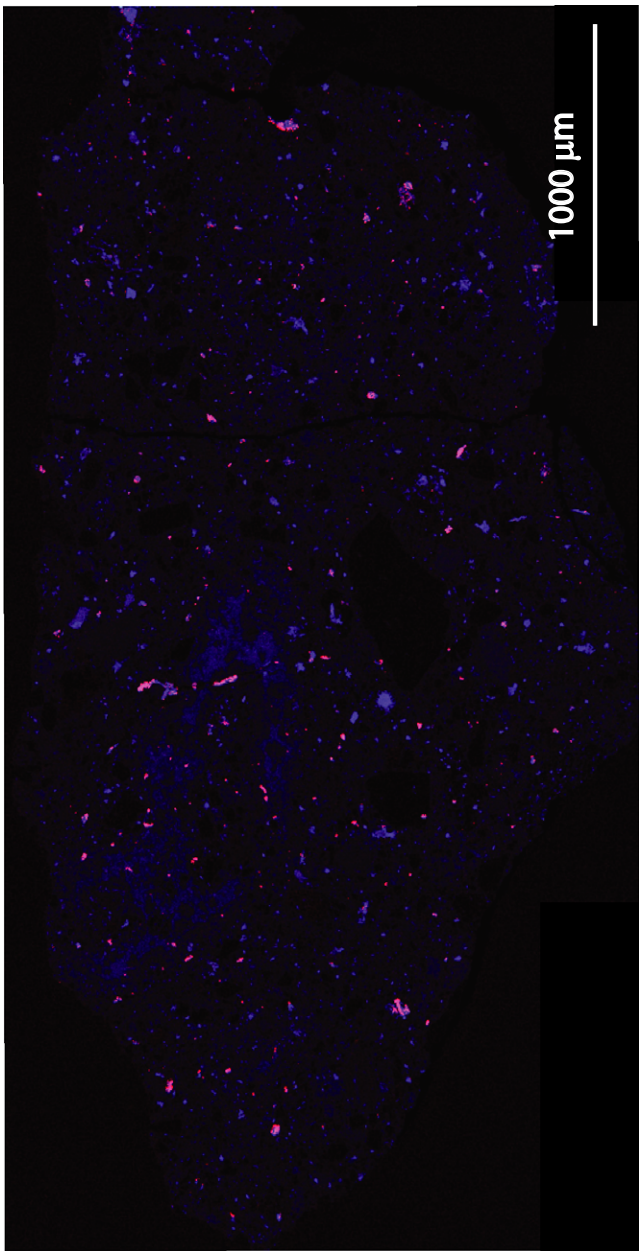

Fig. 3. Coupled S-Fe X-ray intensity map showing the distribution of pyrite (light pink) and Fe (Ti) oxides (dark blue) in the thin section of NWA 7533.

can be firmly identified as being formerly pyrite gave 0.3 ± 0.1% (vol%). Of course, these values are only semiquantitative: considerable errors may come from misidentification of some Fe oxyhydroxides and difficulties in calculating surface areas of some highly denticulated pyrite grains that are finely intergrown with fine-grained Fe-(Ti) oxides. A combined iron-sulfur X-ray map on half of the thin section surface gives a bit higher sulfide content (0.6 ± 0.1 vol% corresponding to 1.0% by weight assuming a density of 5.5 for pyrite and 3 for nonsulfide minerals. Note that Agee et al. (2013) reported 500 ppm S (as 0.1 wt% SO_2) in the bulk-rock analysis of NWA 7034. Laser ablation analyses on ICM and CLIMR gave about 850 ± 200 ppm S (Humayun et al. 2013; supplementary data). These bulk S contents correspond to ~0.1–0.2 wt% pyrite, assuming that pyrite is the only S carrier in NWA 7533 (there are no coupled Ca + S hotspots corresponding to Ca sulfate in X-ray maps). Of course, these pyrite modal abundances based on bulk-rock S abundances are minimum values, as they are not corrected for the effect of alteration on S abundances.

As shown by the combined iron-sulfur X-ray map image of Fig. 3, pyrite is randomly distributed in NWA 7533. In situ LA-ICPMS analyses detected hundreds ppm S in all of the lithologies defined in NWA 7533, i.e., the fine-grained matrix (ICM), clast-laden impact melt rocks (CLIMR), melt spherules, microbasalts, lithic clasts, and mineral clasts (Humayun et al. 2013; supplementary data). Even the latest cracks cutting across the whole meteorite usually contain some pyrite (Fig. 4). The average grain size of pyrite crystals is 30–40 µm. The largest crystals are ~120–150 microns in maximum dimensions while crystal clusters may reach 200 µm in maximum dimensions. NWA 7533 pyrite shows a strong tendency to occur as euhedral crystals (Fig. 2). Perfect cubes are quite rare, as are perfect octahedra. Cubic crystals were observed mostly inside open cracks, low-Ca pyroxene clots, and ICM. The crystal in Fig. 2A was selected for a TEM investigation. Several precession electron diffraction patterns, together with their simulation, confirm the pyrite structure (space group *Pa*3, a = 5.4 Å, Fig. 5A). This pyrite grain is free of crystal defects suggesting that it did not suffer strong shock metamorphism (Fig. 5B). No systematic relationships between pyrite crystal shape and host lithology can be defined. Most crystals show combinations between cubes, truncated cubes, and octahedra (Fig. 2). Regardless of their host lithology, pyrite crystals are invariably fractured and disrupted into subgrains. Fracture networks are evenly distributed, ranging from a few cracks parallel to crystal planes to regularly spaced cell-like systems; in most extreme cases, pyrite crystals were fragmented into particles of <1–2 µm across. Fractures are generally confined to the pyrite alone (i.e., they do not affect neighboring Fe oxides or silicates); some cracks abruptly stop at the interface between pyrite and partly engulfed feldspar microliths. A few pyrite crystals display parallel sets of multiple planar cracks or cleavages producing lozenge-like networks looking like planar features observed in shock metamorphosed rocks (Fig. 2B).

Whether planar or irregular, fracture planes served as preferential pathways for alteration of the pyrite into

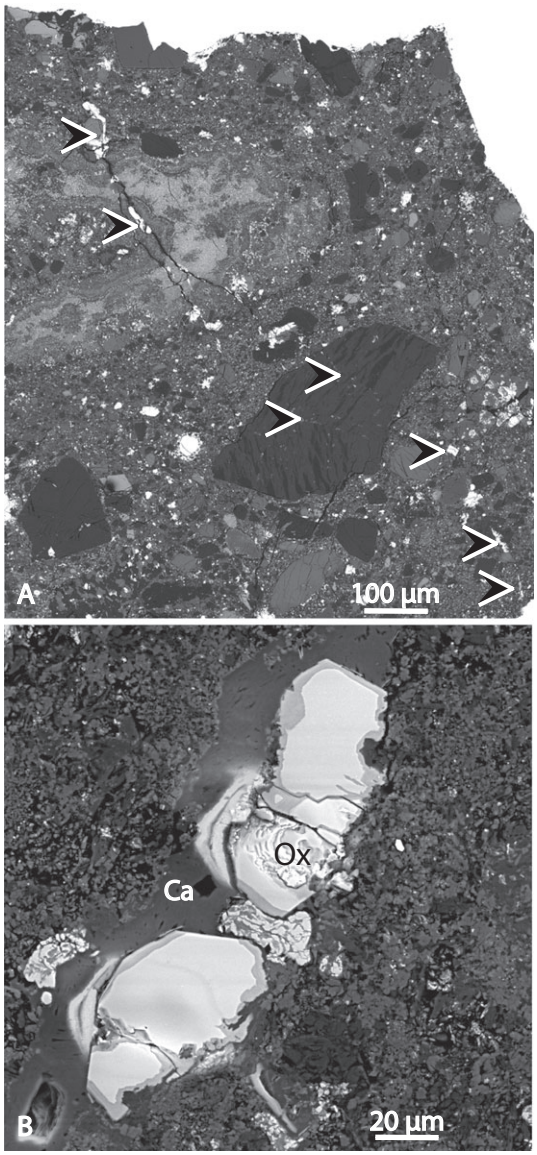

Fig. 4. A) Pyrite-bearing open fractures in the thin section of NWA 7533. Arrows indicate the pyrite crystals. Note that the pyrite-bearing vein cut across all the main lithological components of the meteorite (CLIMR, clasts, ICM). B) Well-preserved (i.e., only slightly fractured) euhedral pyrite inside a calcitized vein (Ca).

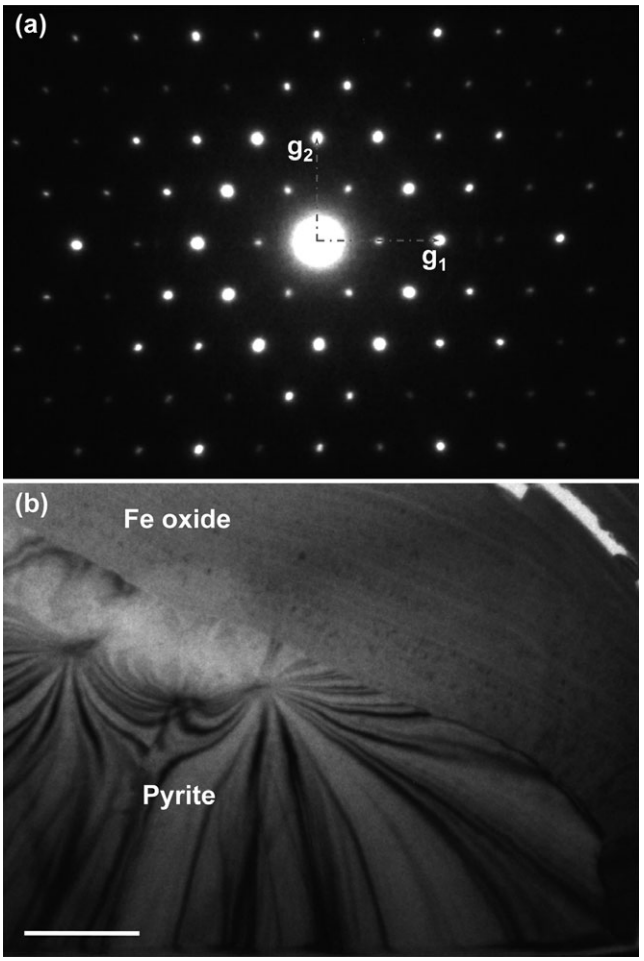

Fig. 5. TEM on the pyrite. A) Selected area precession electron diffraction pattern recorded on the pyrite grain of Fig. 2A (zone axis [111]). g_1 corresponds to (220) reflections and g_2 to (211) reflections. B) Bright field image of the selected pyrite grain and the associated surrounding Fe oxide layer. The grain is free of crystal defect. The dark lines in the pyrite area are due to Bragg contrast (scale bar = 1 µm).

Fe oxyhydroxides. In the case of complete replacement, crack patterns give rise to well-preserved Fe oxyhydroxide pseudomorphs after pyrite showing concentric zoning (Fig. 2C). This alteration is not uniformly distributed over the six polished sections studied. Section 1 (the closest to the fusion crust) is the most altered: the hundred or more pyrite grains identified over the whole section are almost completely altered (Fig. 6). Fe oxyhydroxide pseudomorphs preserve a few relict pyrites. Sections 2 and 5 are the least altered while the other sections show alteration gradients from one side to another. Detailed TEM study on the crystal of Fig. 2A shows that the interface between pyrite and its replacement material is curved without any roughness (Fig. 7A). The altered area is composed of grains with a size of a few tens of nanometer. Selected area diffraction patterns show thin rings with d-spacing close to 2.7 and 1.5 Å for the two most intense rings which correspond to the main diffraction lines of Fe oxides and Fe oxyhydroxides. There are strong variations of intensity within the rings revealing preferential crystallographic orientations of the nanocrystalline grains (see insert in Fig. 7A). Diffraction patterns also show variation at the submicron scale, depending on the investigated areas. This is probably mainly due to local textural

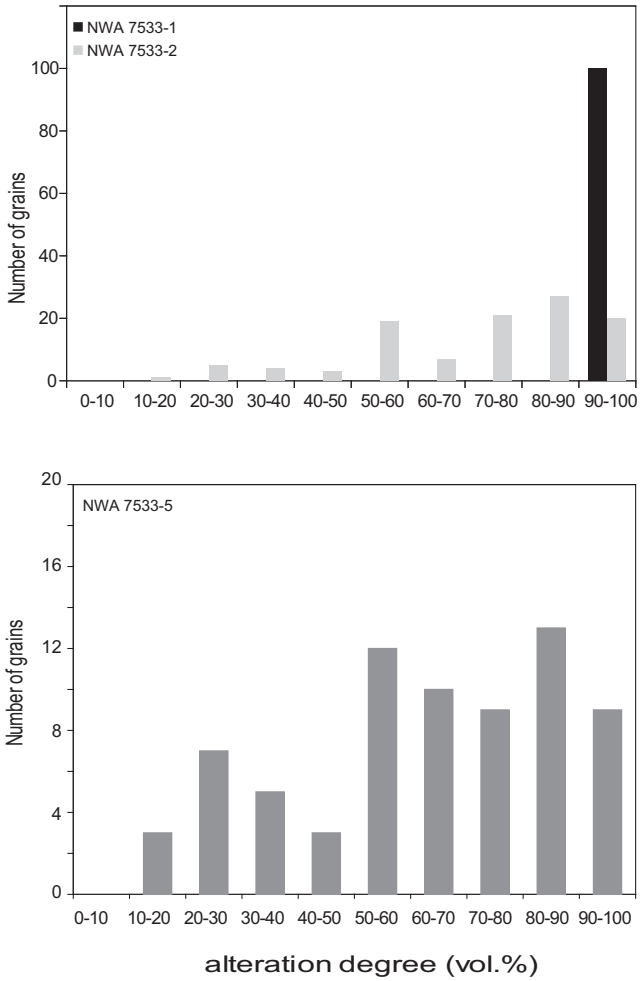

Fig. 6. Histograms showing the alteration degree of pyrite in three polished sections of NWA 7533 (visual estimations from BSE images). Section 1 pyrites are the most altered. Sections 2 and 5 show an alteration gradient from one side to the other, resulting in two pyrite populations with respect to Fe oxyhydroxide alteration.

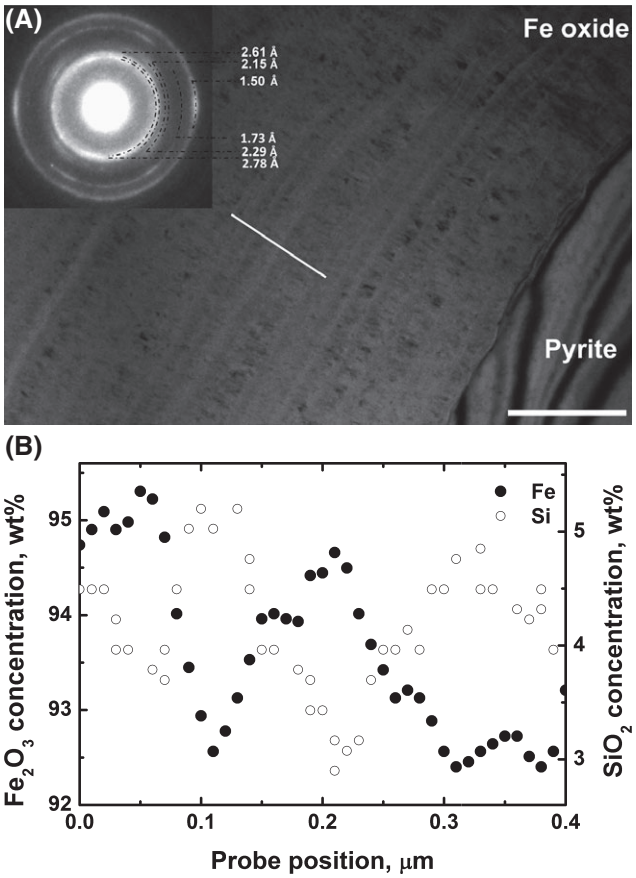

Fig. 7. TEM of the interface between the pyrite grain and the iron-oxide. A) Bright-field image showing the alternating layers more or less dark in the iron-oxide surrounding the pyrite grain. These layers are parallel to the interface with the pyrite and correspond to variations of composition. The scale bar = 0.5 μm. A selected area electron diffraction pattern recorded on the iron-oxide area is shown in insert. Note the preferential orientation of the nano-grains, as revealed by the wide variations in intensity on the diffraction rings. B) EDS-TEM composition profile across alternating layers bright (enriched in SiO_2) and dark (depleted in SiO_2) layers in the iron-oxide area (the direction of the profile is indicated by a white line).

orientations of the nano-grains but also possibly to the presence of different Fe oxide and/or Fe oxyhydroxide phases across studied altered areas. These complexities, coupled with closely similar electron diffraction patterns for the various Fe oxide–hydroxides, make a clear identification of the pyrite alteration product difficult by electron diffraction.

CLIMR pyrite crystals are preferentially located inside clots that are made from radiating fibrous orthopyroxene plus Fe-(Ti) oxides surrounded by polycrystalline microlithic plagioclase. Pyrite in pyroxene clots frequently occurs as euhedral crystals with sharp margins. It is usually located inside the clot but also overlapping clot-melt rock contacts (Fig. 2B). Pyrite clearly postdates the fibrous textured pyroxene because this latter may be completely isolated inside poikilitic pyrite. Haloes depleted in fine-grained Fe oxides are commonly observed around pyrite. Not all pyrite in CLIMR are hosted in clots. Some crystals may be scattered within plagioclase–pyroxene microlithic groundmass. Pyrite in finely devitrified melt spherules is scattered inside fracture planes that radiate across the spherules. Such crystals are inclusion-free octahedra or cubooctahedral crystals.

Pyrite crystals are most common in ICM, generally occurring as isolated crystals, but clusters of several crystals, as well as anhedral polycrystalline masses up to 200 μm in maximum dimensions can also be observed at contacts between ICM and lithic or mineral clasts.

Section 5 ICM is pierced by open voids, a few mm in depth, providing three-dimensional views of unusually big pyrite crystals (200 μm). The latter display a wide variety of crystal shapes ranging from octahedra, cubo-octahedra, and complex polysynthetic parallel growth faces ending up with pentagonal faces (Fig. 2D). Void walls are deeply calcitized fine materials. Pyrite crystal faces are irregular and embayed by fluffy ICM minerals (pyroxenes, plagioclase). Many ICM-hosted pyrite crystals show denticulated margins (Figs. 2E–J) in addition to trapping the greatest diversity of mineral inclusions covering the whole range of matrix and clast minerals. Ca-rich and Ca-poor pyroxene; feldspar, either K-rich or Na- and Ca-rich; as well as perfectly euhedral apatite, Fe oxides, ilmenite, rutile, zircon, and baddeleyite inclusions have been identified inside ICM pyrites, in addition to a few submicrometric inclusions of thorianite ($ThSiO_4$) and Os-Ir-rich phases. Except for apatite, none of those mineral inclusions inside pyrite show well-defined crystalline shapes or preferred orientation with respect to host pyrite (e.g., Fig. 2F). Ilmenite inclusions are sometimes surrounded by Fe-depleted rims a few microns thick that are identified as a TiO_2 compound by EDS (Fig. 2G). All intermediate steps of matrix mineral entrapment by pyrite can be observed, from partly "attached" plagioclase/Ca pyroxene microclasts to highly poikiloblastic pyrite. Such microtextures indicate partial entrapment of very fine matrix mineral dust by growing pyrite. In some cases, the ICM mineral dust seems to be pushed away by pyrite, forming a kind of polycrystalline halo around the pyrite (Fig. 2F). Highly elongated polycrystalline pyrite aggregates, up to several hundreds of micrometers in length, display highly denticulated margins, due to partial entrapment of ICM grains. One of these ribbons, about 150 μm in length, was identified by SEM as a polycrystalline pyrrhotite vein. Vein-like pyrite occurs inside major fractures cutting the meteorite. Pyrite-bearing open fractures can be tracked over several millimeters in two of the six sections studied so far (Fig. 4). Pyrite crystals that obstruct such open fracture planes (now calcitized) running across all the main lithological components of the meteorite (CLIMR, clasts, ICM) are clusters and chains of well-preserved (i.e., only slightly fractured) euhedral pyrite devoid of any inclusions (Fig. 2H).

Pyrite also occurs inside mineral and lithic clasts, clearly crosscutting the different clasts. In monomineralic clasts, the pyrite is present inside cracks, often as clusters of crystals. A few low-Ca pyroxene clasts have been found to be invaded and partly replaced by pyrite that infiltrates cleavage planes in the pyroxene (Fig. 2I). Note that this replacement is pseudomorphic, i.e., the shape of original pyroxene clast was preserved, and fracture planes affect both pyrite and low-Ca pyroxene. Noritic and monzonitic clasts are also pyrite-bearing. Pyrite occurs as secondary overgrowths on magnetite–ilmenite oxide grains. Pyrite is almost lacking in coarse-grained lithic clasts that do not show extensive fracturing. The same is also true for microbasalts; every pyrite grain detected is connected to sealed fracture planes. This is shown among other evidence by partial alteration of the pyrite to Fe oxyhydroxides.

Regardless of its shape and crystallization sites, pyrite is almost invariably associated and/or intergrown with micron-sized Fe-(Ti) oxides identified as magnetite–maghemites. These are associations of pyrite and oxides crystallized side-by-side (e.g., CLIMR-hosted clots; Fig. 2B), pyrite intergrown with oxides that served as nuclei for pyrite crystallization (i.e., Fig. 2E), and residual skeletal oxides isolated in the middle of pyrite crystals (Figs. 2C and 2F). Even the late fractures now filled up with calcite display sulfide-oxide composite grains (Fig. 2H). Finely divided clasts of low-Ti magnetite + ilmenite + apatite (+ rutile) may be totally cemented by pyrite, now partly replaced by alteration products. High-magnification scanning allowed the detection of platinum-group element (PGE) micronuggets in one of these sulfide-oxide composite grains. These are very small-sized (300–700 nm) particles now hosted in Fe oxyhydroxides, except for one grain that appears to be inside apatite (Fig. 8). EDS spectra have been collected for two (A and B) of the four nuggets, despite considerable noise from host Fe oxyhydroxides and apatite. PGE micronuggets were identified by using high acceleration voltage (20 kV) and both L alpha and M alpha X-ray lines to avoid peak overlaps with major elements of the pyrite and its alteration product or apatite. This analytical technique provided reliable results for identification of micrometer-sized platinum-group minerals included in Fe-Ni sulfides, both in terrestrial mantle rocks (Lorand et al. 2010) and Martian meteorites (Lorand et al. 2012). Nugget A included in apatite is an Ir-(Os)-As-S compound; Nugget B is Os-S-rich (Fig. 8).

PHASE CHEMISTRY

The 140 grains analyzed with the standardless semiquantitative SEM–EDS procedure confirm the FeS_2 stoichiometry (Fe/S atomic ratio = 0.5, Fig. 9), as does the TEM–EDS microanalysis performed on the crystal of Fig. 2A. NWA 7533 pyrites display a wide range of Ni contents, from undetectable (<0.5 wt%) concentrations, up to 4.5 wt%, regardless of their location in NWA 7533 lithologies. About one-third of the 350 pyrite analyses show Ni > 0.5 wt% (Fig. 9). The

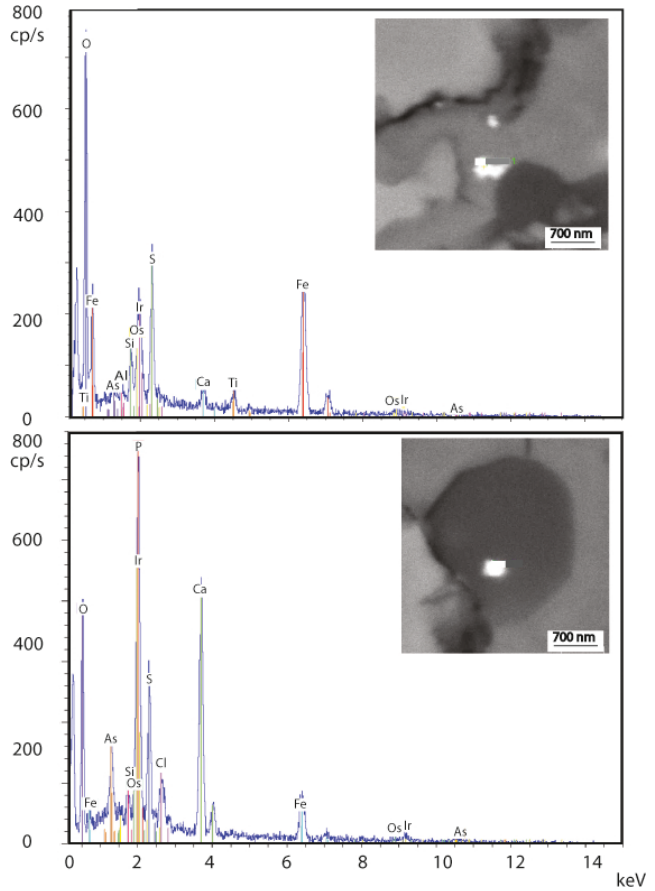

Fig. 8. Small-sized (300–700 nm) highly siderophile element-rich microparticles hosted in pyrite. Nugget A is an Ir-(Os)-As-S compound included in apatite; Nugget B is a Os-S-rich compound hosted in pyrite alteration products. The EDS-SEM spectra were collected at 20 kV (see text for details).

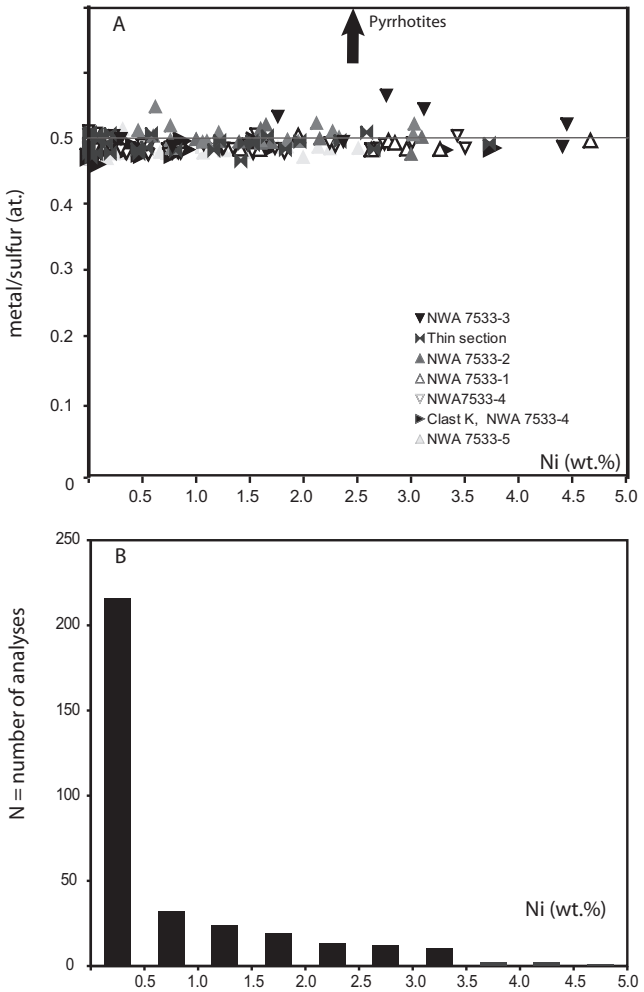

Fig. 9. Nickel concentrations in pyrite (standardless EDX analyses). The average metal/sulfur ratio (0.5) corresponds to Fe disulfides; the few analyses that show metal excess come from strongly altered pyrite grains. About one-third of the total number of analyzed grains show Ni > 0.5 wt%.

occurrence of Ni in pyrite was confirmed by synchrotron maps (Bland, personal communication) and EMP analysis. EMP WDS analyses agree quite well with SEM semiquantitative data, in spite of different beam sizes and correction procedures (Fig. 10). Most if not all Ni-rich pyrite grains show highly heterogeneous distribution of Ni. Nickel-rich spots can be observed in euhedral grains. Anhedral grains display a Ni-rich inner zone showing uniformly high Ni content, surrounded by Ni-free pyrite overgrowths. Nickel-rich zones are separated from Ni-poor areas by sharp and well-defined boundaries, obviously further opened by late fracturing (Figs. 2J and 2K). On average, the Ni-enriched areas are quite easily detected in reflected light optical microscopy by their much lower degree of alteration to Fe oxyhydroxides; some Ni-rich pyrite may be alteration-free, while adjacent Ni-poor pyrite is heavily replaced. Thus, the diagram of Fig. 9 is biased by this differential alteration: the Ni-poor pyrite is likely underrepresented because many crystals were too altered to be probed.

Among trace elements, pyrite contains some Co (up to 1800 ppm; Table 1). A few analyses may define a loosely constant Ni/Co around 10, reminiscent of meteoritic metal compositions; otherwise, Ni and Co do not correlate at all (Fig. 11). Se concentrations were above detection limit (64 ppm) only in the Ni-rich grains that contain up to 170 ppm Se. Regardless of Ni contents, Cu and Zn contents are close to or below detection limits (<77 and <91 ppm, respectively), as are As contents (<117 ppm), except occasional concentration peaks up to 600 ppm (Table 1). Higher (>1.000 ppm As) As contents are ruled out by the S contents that are, within error, very akin to the theoretical value calculated for stoichiometric pyrite (53.4 wt%) (Qian et al. 2010).

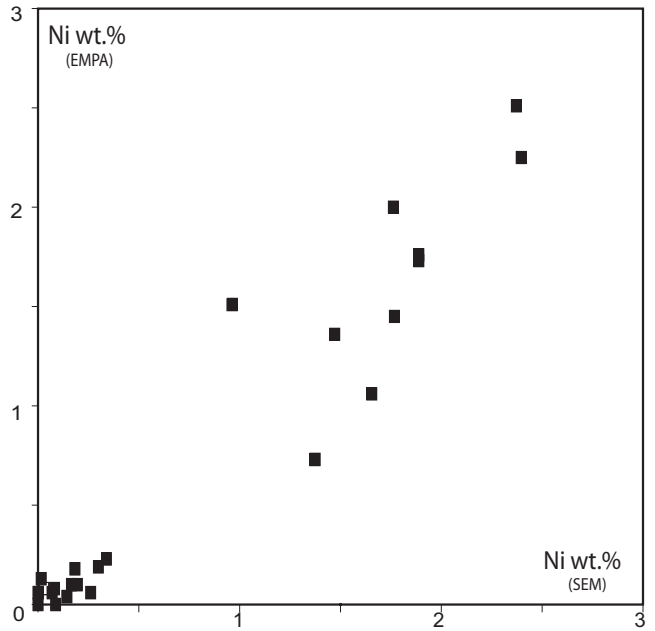

Fig. 10. Comparison between EDS (SEM) and WDS (EMP) analyses of Ni.

The only ICM-hosted vein-like pyrrhotite identified over the six sections is Ni-bearing, although its Ni concentration range (0–1.9 wt% Ni) defined over four standardless EDS analyses is more restricted than that of pyrite (Table 1).

EMP analyses of pyrite alteration products give total oxide contents similar to ferric oxyhydroxide compositions (88.6 wt%; Table 2). The other chemical components detected in pyrite is silica (4 wt%) in addition to minor amounts of MgO, CaO, NiO, and S. EDS-STEM analyses also confirm the presence of all of these minor elements (Table 2). However, TEM images also revealed an alternation of dark and bright layers, parallel to the interface with pyrite, with a wavelength ranging from 50 to 200 nm (Fig. 7A). Bright layers are found to be enriched while dark layers are SiO_2-poor, compared to the average composition. Figure 7B shows an EDS-STEM composition profile across a few alternating layers. The high and low concentration values of SiO_2 are 5.2 and 2.9 wt% oxide, respectively, with an average at 3.9 wt%, in agreement with the mean EMP analyses. The low total oxide content is indicative of a high water content as expected for minerals from the series goethite–akaganeite–lepidocrocite. Whether this putative water deduced from EMP analyses is located inside oxyhydroxide sublattice or occurs as adsorbed impurities (e.g., H_4SiO_4; Song et al. 2013) is unclear from the present EMP and TEM analyses. Using high-resolution TEM (HRTEM) analysis coupled with electron diffraction, Muttik et al. (2014b) identified the alteration rinds around an undetermined sulfide (previously identified as troilite in Muttik et al. 2014a) in NWA 7034 as concentric bands of maghemite that are composed of closely packed small nanoparticles. By contrast, our electron diffraction analyses were inconclusive for discriminating Fe (oxy)hydroxides in NWA 7533. Moreover, maghemite can incorporate only up to 2 wt% H_2O in its structure (as protons on the vacant octahedral sites) (Cornell and Schwertmann 1996), which is far too low compared to the strong deficit in our EMP analyses (~11 wt%). Gattacceca et al. (2014) identified by Mössbauer analysis of NWA 7034 a superparamagnetic göethite phase which, according to Muttik et al. (2014a, 2014b), more likely corresponds to nanometer-sized Fe oxide/hydroxide that occurs between the coarser-grained maghemite particles in the fine-grained matrix. There are two possibilities to reconcile such widely diverging results: either all EMP analyses of NWA 7533 pyrite alteration products are mixtures of hydroxylated Fe oxides, a silica-rich phase and probably pores, to get the totals down (the resemblance to goethite would be a coincidence) or the pyrite alteration products show significantly different mineralogy between NWA 7034 and NWA 7533, i.e., between troilite alteration products and pyrite alteration products.

NanoSIMS imaging of five grains (ICM-hosted and vein pyrite) indicates that Fe oxyhydroxides replacing the pyrite exhibit a homogeneous D/H ratio (δD value = 10 ± 85‰). Even assuming our terrestrial standard to have a 250‰ error bar (i.e., its ratio is lying somewhere between the most extreme endmembers recognized on Earth [−400 to +100‰]), the NanoSIMS data clearly show that the alteration products are within the terrestrial range (i.e., a similar ratio to the terrestrial goethite; Fig. 12).

DISCUSSION

Martian Pyrite

The pervasive distribution of pyrite throughout all of the lithologies defined in NWA 7533 and its paired samples (e.g., NWA 7455) is a unique feature among Martian meteorites. Pyrite was interpreted as a secondary alteration phase that occurred on Mars from localized, low-temperature aqueous alteration of clast component under reducing conditions (Wittmann et al. 2015). The chemical data, the planar features, and the extensive fracturing of pyrite in NWA 7533 clearly argue for a Martian origin, as do evidence of high-T elemental diffusion (Fe), and high Ni contents (see below). Pyrite fracturing likely dates back to the weak shock event that liberated the meteorite from the

Table 1. Representative electron microprobe analyses of NWA 7533 pyrites (SEM data in italics).

Major elements						
wt%	1/1.8c	3/1.	8/1.3c	11/1.6C	16/1.15C	20/1
Fe	44.43	45.98	42.96	45.81	45.06	45.96
Ni	1.85 (*1.76*)	0.19 (*nd*)	2.77	0.07 (*0.06*)	1.45 (*1.36*)	0.23
S	53.31	53.36	53.85	53.75	53.5	53.44
Total	99.62	99.62	99.58	99.65	100.02	99.64
Trace elements (wt%)						
Ni	1.95	0.268	2.365	0.100–0.091	1.221	0.197
Co	b.d.l.	b.d.l.	0.13	b.d.l.	0.01	b.d.l.
Cu	b.d.l.	0.009	b.d.l.	b.d.l.	b.d.l.	b.d.l.
Zn	b.d.l.	b.d.l.	b.d.l.	b.d.l.	b.d.l.	b.d.l.
Se	0.017	0.008	0.017	0.008	0.014	b.d.l.
As	b.d.l.	0.058	b.d.l.	b.d.l.	0.011	0.018
Pb	b.d.l.	b.d.l.	b.d.l.	b.d.l.	b.d.l.	b.d.l.
Major elements						
wt%	35.1	29.1	5.14 1	5 26 23A	5 23 17A	5 16 6A
Fe	43.70	44.67	46.23	46.57	45.43	45.26
Ni	2.32 (*2.51*)	2.50	b.d.l.	0.03 (*0.05*)	0.75	1.52 (*1.28*)
S	53.84	53.02	53.66	53.56	53.25	53.5
Total	99.85	100.79	99.91	100.15	99.43	100.27
Trace elements (wt%)						
Ni	2.26	2.64	0.010	0.011	0.920	0.613
Co	0.014	b.d.l.	0.015	0.021	b.d.l.	0.013
Cu	b.d.l.	b.d.l.	b.d.l.	b.d.l.	b.d.l.	0.009
Zn	b.d.l.	b.d.l.	b.d.l.	b.d.l.	b.d.l.	b.d.l.
Se	na	na	b.d.l.	b.d.l.	0.007	0.0064
As	na	b.d.l.	0.011	b.d.l.	b.d.l.	b.d.l.
Pb	na	b.d.l.	b.d.l.	0.05	b.d.l.	b.d.l.
Major elements						
wt%	5 16 5A	5/1. 12C	10/1.5C	15.1	22/1.18c	30/1.22C
Fe	44.31	46.11	46.04	44.98	44.72	45.67
Ni	2.22 (*0.66*)	0.18 (*0.18*)	0.26	0.84	1.73 (*2.0*)	1.36
S	53.3	53.34	53.20	53.64	52.90	53.01
Total	99.84	99.64	99.47	99.47	99.11	100.05
Trace elements (wt%)						
Ni	1.17	0.40	0.150	0.797	1.922	1.360
Co	0.045	0.016	b.d.l.	0.019	0.01	0.013
Cu	b.d.l.	0.009	b.d.l.	b.d.l.	b.d.l.	b.d.l.
Zn	b.d.l.	b.d.l.	b.d.l.	b.d.l.	b.d.l.	b.d.l.
Se	0.0087	b.d.l.	0.0081	0.012	0.012	0.011
As	0.014	0.058	0.01	b.d.l.	0.0119	b.d.l.
Pb	0.05	b.d.l.	0.05	0.05	b.d.l.	b.d.l.

Analytical conditions for the trace element procedure: Kα line for Cu, Zn, Co, Ni; Lα line for Se; Lβ line for As; and Mβ line for Pb. Sample current = 250 nA. Counting time 60 s peak, 60 s background; each element but Pb counted twice, on two spectrometers (Se and As on TAP crystals [Sp1 and Sp4]; Ni, Co, Cu, Zn on LIF crystals [Sp 3 and Sp5]; Pb on PET crystal [Sp2]. Concentrations calculated with pure metal standards for Ni, Co, Cu, Se; ZnS for Zn; AsGa alloy for As; pyrite for S and Fe; PbS for Pb. Mean detection limits (wt%): Ni: 0.01; Co: 0.0068; Cu: 0.0077; Zn: 0.009; Se: 0.0064; As: 0.012; Pb: 0.05. b.d.l. = below detection limit. n.d. = not determined.

Martian subsurface crust. There are virtually no data on shocked pyrite in meteorites as pyrite is almost unknown in this context. By analogy with quartz, planar elements in pyrite could correspond to planar fractures or planar deformation features (PDFs). The latter develop in quartz at relatively low pressures of shock metamorphism (S0–S1 stage corresponding to shock pressures below ~10 GPa; French 1998; Stöffler and Grieve 2007). The NWA7533 pyrite is free of crystal defects, as revealed by TEM, suggesting that it suffered only very soft shock metamorphism consistent with mild launch conditions (<15 Gpa and >5 Gpa) that Wittmann et al. (2015) estimated for NWA 7455 from pyroxenes and feldspar deformation features. Pyrite

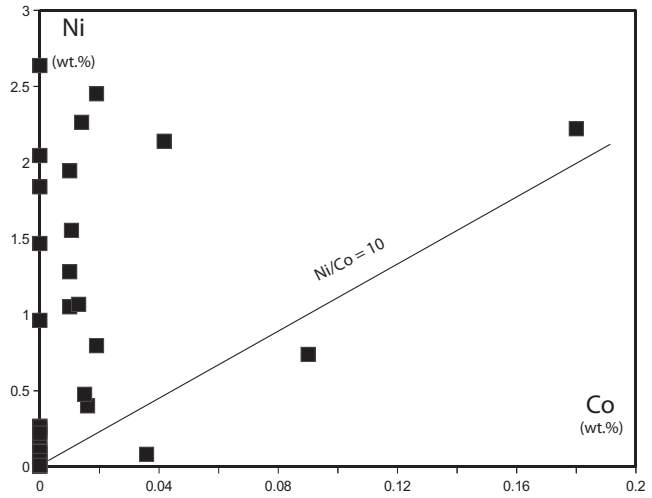

Fig. 11. Ni versus Co diagram for NWA 7533 pyrite (trace element analytical procedure).

Table 2. Composition (wt%) of Fe oxyhydroxides replacing pyrite. The table includes a mean composition determined by EMPA (average on 15 analyses) and local compositions recorded by EDS-TEM on the alternating dark and white layers (uncertainties given in parentheses at 2σ). For EDS, data are normalized at 100%.

EMPA + SD		*Low-SiO_2	*High-SiO_2	*Bulk (1*1 μm)
SiO2	4.59 (0.64)	2.88 (0.20)	5.21 (0.22)	3.18 (0.10)
Al_2O_3	0.02 (0.02)	b.d.l.	b.d.l.	b.d.l.
TiO_2	0.15 (0.15)	b.d.l.	b.d.l.	b.d.l.
Cr_2O_3	0.02 (0.05)	b.d.l.	b.d.l.	b.d.l.
Fe_2O_3	80.94 (2.77)	95.3 (1.8)	92.4 (2.0)	94.7 (0.8)
MnO	0.07 (0.06)	b.d.l.	b.d.l.	b.d.l.
MgO	0.67 (0.30)	0.83 (0.18)	0.50 (0.12)	0.60 (0.08)
CaO	0.95 (0.20)	0.58 (0.08)	1.13 (0.12)	0.85 (0.06)
Na_2O	0.02 (0.04)	b.d.l.	b.d.l.	b.d.l.
P_2O_5	0.13 (0.05)	b.d.l.	b.d.l.	b.d.l.
SO_2	0.42 (0.26)	0.38 (0.10)	0.50 (0.12)	0.49 (0.06)
NiO	0.58 (0.78)	b.d.l.	0.21 (0.08)	0.16 (0.04)
Total	88.56	100.00	100.00	100.00

exhibits an extremely brittle behavior resulting in cataclastic deformation, favored by coarse-grained crystal size. One may note that at temperatures up to 400 °C and confining pressures up to 1000 MPa, pyrite strain rates range between 10^{-4} to 10^{-7} s^{-1} (McClay and Ellis [1983] and references therein). By comparison, shock strain rates involved in shock metamorphism are in the range 10^4 to 10^7 s^{-1} far beyond the values for pyrite. This huge difference in critical strain rate indicates that pyrite will behave brittly even for the softest launch conditions, as evidenced by NWA 7533. Shock wave intensities beyond 50 GPa, as observed in some SNCs (e.g., NWA 2737) would have resulted in pyrite decomposition into troilite and Fe-Ni metal, so this reaction produces sulfur vapor and S loss (Yamaguchi et al. 1999; Lorand et al. 2012).

Martian Versus Terrestrial Pyrite Alteration Products

Of course, the oxidation of pyrite is a postshock event as it is closely driven by fracture networks, whether planar or other fracture patterns. This simple observation is the strongest evidence for assuming a terrestrial origin of pyrite-replacing Fe oxyhydroxides that have preserved delicate, concentrically zoned microtextures free of fracture planes. A terrestrial origin is also supported by δD values within the terrestrial range. It also accounts for the pyrite alteration gradient detected between section 1 and the other sections investigated which were cut closer to the interior or the meteorite. Sulfide alteration is common in hot desert finds, including shergottite finds from Saharan deserts (Lorand et al. 2005). Pyrrhotite or pyrite are altered by oxygenated surface water into water-soluble sulfates while insoluble oxidized iron (Fe^{3+}) is fixed as Fe oxyhydroxides by the following reactions.

$$FeS_2 + 15/2O_2 + 7/2H_2O = 2SO_4^- + Fe(OH)_3 + 4H^+$$

$$FeS_2 + 7/2O_2 + H_2O = FeSO_4 + H_2SO_4$$

(Jerz and Rimstidt 2004; pH>2).

Pyrite alteration reactions should produce Fe hydroxide (ferrihydrite) which is supposed to be metastable and rapidly replaced by another goethite-like phase or iron oxides (hematite), depending on pH and T conditions postdating alteration (Cudennec and Lecerf 2006). For NWA 7533, the compositional features of Fe oxyhydroxides (up to 4 wt% Si, coupled with trace amounts of Ca and Mg; Table 2) indicate incipient alteration of silicates such as high Ca pyroxene and plagioclase (the ICM and CLIMR components), as expected from highly acidic sulfate-producing terrestrial weathering (e.g., Fernandez-Remolar et al. 2004; Durocher and Schindler 2011; Moncur et al. 2009). It is well known from sulfide mine tailings that milling and grain size reduction increases the rate and susceptibility of iron-bearing phases to oxidation processes (Pratt et al. 1996; Nesbitt et al. 1998). Extensive fracturing and grain size reduction also increased the extent of pyrite alteration in NWA 7533. Pyrite relicts were preserved inside altered crystals thanks to Fe oxyhydroxides that created a passivation layer (Huminicki and Rimstidt 2009) and to Ni, as shown by the lower alteration degree of high-Ni pyrite cores. Transition metals such as Ni increase significantly the

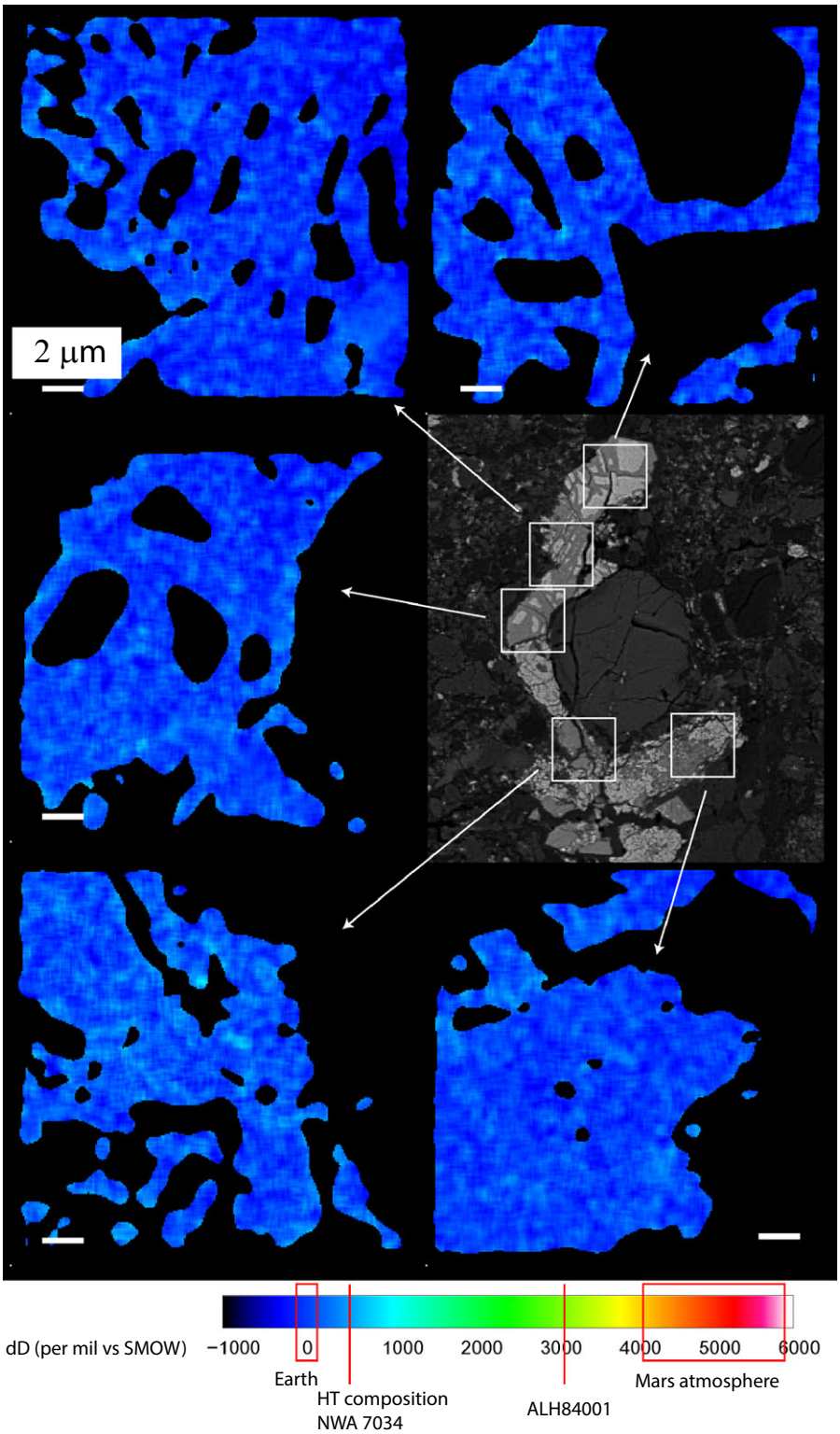

Fig. 12. NanoSIMS δD (versus SMOW) images of the alteration products of NWA 7533 pyrite. Their isotopic signature confirms a terrestrial origin, for Fe oxyhydroxides. Shown for comparison are: the isotopic composition of Mars atmosphere, determined by SAM on board the MSL rover (Webster et al. 2013), of apatites in ALH 84001 (Greenwood et al. 2008) and of the high temperature component of NWA 7034 (paired with NWA 7534, Agee et al. 2013); note that the bulk composition of NWA 7034 is very close to the terrestrial value, suggesting a significant effect of terrestrial Fe oxyhydroxides in the D/H budget of Martian breccias (Agee et al. 2013).

weathering resistance of Fe-Ni alloys in meteorite samples (Lee and Bland 2004) and NWA 7533 suggests that they acted similarly for pyrite.

There is also ample evidence that highly acidic sulfate-producing weathering also occurred on Mars as well. This alteration was recognized in Hesperian soils to generate low pH sulfuric acid-rich environments dissolving olivine and apatite at low water/rock ratios while preserving pyroxene and plagioclase (e.g., Tosca et al. 2004; Hurowitz et al. 2010). Sulfide alteration products are ferric iron–sulfates (such as jarosite) coexisting with ferric iron oxides (Zolotov and Shock 2005; Dehouck et al. 2012). If such alteration had occurred in NWA 7544, it necessarily postdated the 1.4 Ga resetting event that likely generated the pyrite, i.e., under conditions of ephemeral water corresponding to dry Mars. Pyrite alteration products should bear evidence of the extreme δD (around 4000) of the modern Mars atmosphere (Webster et al. 2013), which lies well beyond the analytical uncertainty of our nanoSIMS analyses. There is no evidence for highly acidic conditions similar to those documented for Hesperian rocks (pH <4–5; Hurowitz et al. 2006; Chevrier et al. 2004, 2006; Dehouck et al. 2012) in NWA 7533 as it lacks marcasite, Fe-Mg sulfates, altered K-feldspar or altered apatite, or Zn and Cl enrichments (Humayun et al. 2013, 2014). To summarize, the lack of any geochemical or mineralogical evidence of Martian alteration products in NWA 7533 pyrite led us to consider the terrestrial origin more likely for those pyrite alteration products.

The net effect of alteration was to remove most of the S originally present as pyrite. Assuming that no other S-rich minerals are present in NWA 7533, prealteration pyrite modal abundances correspond to bulk S contents of at least 2500–3000 ppm and up to 5400 ppm. The sharp difference between these estimated S contents and the measured ones (500–1000 ppm) indicates that terrestrial alteration may have leached up to 90% of the initial S budget; our conclusion is supported by pyrite S/Se ratios which are chondritic to higher compared to bulk-rock estimates (3000–8000 versus ~1000; Humayun et al. 2013; supplementary data). Meteorites that experienced hot desert alteration generally display similar S losses (e.g., Dreibus et al. 1995).

Temperature–fO_2–pH–Eh Conditions of Pyrite Precipitation

Previous reports of pyrite from Martian meteorites (e.g., ALH 84001; Chassigny and some nakhlites) repeatedly concluded that igneous pyrrhotite was largely converted to pyrite through secondary alteration processes, such as impact-driven hydrothermal system (Shearer et al. 1996; Scott 1999; Greenwood et al. 2000; Franz et al. 2014). Pyrrhotite occurs sparsely in NWA 7533 and paired samples ("Troilite" in NWA 7034; Muttik et al. 2014a; low-Ni pyrrhotite of undetermined origin inside an ophitic microbasalt clast in NWA 7455; Wittmann et al. 2015). The pyrrhotite identified in NWA 7533 (Fig. 4) occurs as an anhedral spongy vein inside ICM, in a microtextural site very similar to vein-like pyrite. One may surmise that it is hydrothermal pyrrhotite that was in disequibrium with the overall oxidizing conditions prevailing during final assembly of the breccia. The strongly euhedral shape of NWA 7533 pyrite and its occurrence as disseminated isolated crystals remote from pyrrhotite, both suggest direct growth from sulfur-rich solutions/fluids. Sulfur/selenium ratios of 3000–8000 in these grains are in the accepted range for hydrothermal sulfides (Huston et al. 1995; Luguet et al. 2004). Pyrite thermal stability is limited to T max = 743 °C at 1 bar (Vaughan and Craig [1978] and references therein). Solid solution toward the NiS_2 endmember decreases from ~20 mole% at 600 °C to 10–11 mole% at 500 °C (Vaughan and Craig 1978), the maximum content analyzed in some NWA 7533 pyrite. The Ni-rich domains inside NWA 7533 pyrite grains always have pyrite stoichiometry and their crystalline shapes and optical properties are those of pyrite. Hence, the maximum T for pyrite crystallization in NWA 7533 is <500 °C from the maximum Ni contents; however, Ni-rich pyrites are always overgrown by Ni-free pyrite (but not the opposite) suggesting that pyrite crystallized over a temperature range which cannot be accurately defined but high enough for creating Fe-diffusion haloes on a micrometer scale inside Ca pyroxene coronas and Fe-depleted TiO_2 haloes around ilmenite inclusions. Pyrite is oxidized relative to pyrrhotite (Craig and Vokes 1993) and its widespread distribution in NWA 7533 compared to pyrrhotite is consistent with the overall oxidized conditions recorded by all NWA 7533 lithologies compared to other SNC meteorites (FMQ + 2 log units; Hewins et al. 2014b). The assemblage pyrite–magnetite points to fO_2 conditions more than 3 log units above the reference FMQ buffer curve at 600 °C (Fig. 13). Likewise, noritic clasts that contain low-Ca pyroxene + chromite + pyrite indicate minimum log fO_2 > FMQ + 2 log units. Regarding Eh–pH conditions, pyrite is stable over a wide range of conditions, from acidic conditions for hematite–pyrite assemblages to mildly alkaline for pyrite–magnetite–pyrrhotite assemblages (Rickard and Luther 2007; Qian et al. 2010; Fig. 14). Magnetite–pyrite replacement textures indicate pH conditions >6 at 300 °C and <10, in agreement with the lack of carbonates of Martian origin in NWA 7533 (Fig. 14). Redox conditions were quite similar during lithification in Sheepbed mudstone, the lowermost observed member of the Yellowknife Bay

formation at Gale crater, that shows both pyrrhotite (1 ± 0.5 wt%) and pyrite coexisting with magnetite (Vaniman et al. 2013).

Indirect Impact Contamination in NWA 7533 Pyrite

The high-Ni concentration spots are one of the most remarkable features of NWA 7533 pyrite. The few hydrothermal pyrites so far described in Martian meteorites contain less than 2–3 wt% Ni (Lorand and Chevrier, unpublished data; Scott 1999), as do terrestrial hydrothermal pyrites from Ni-rich serpentinized peridotites (e.g., Luguet et al. 2004; Lorand and Alard 2011). Likewise, Ni-Fe oscillatory zoning so common in hydrothermal pyrite (Herzig and Hannington 1995; Hannington et al. 1998) is lacking in NWA 7533 pyrites. These Ni pyrite occurrences add new evidence for the overall Ni enrichment of regolith breccia meteorites compared to the SNC group. Theoretical modeling has suggested that early volcanism on Mars occurred under more oxidizing conditions than the shergottites, consistent with ≥QFM oxygen fugacities (e.g., Tuff et al. 2013). Under these oxidizing conditions, the crustal rocks can have higher abundances of Ni because Ni solubility in the oxidized melts is much higher. In that model, it is unclear how Ni was transferred from a priori homogeneous crustal rocks at magmatic temperature to heterogeneous pyrite at hydrothermal temperature. The wide range of Ni concentrations, at a micrometer scale is more consistent with occasional Ni contamination of growing pyrite crystals by exotic micron-sized Ni-rich meteoritic particles now widely distributed in the meteorite, due to repeated impacts (Humayun et al. 2013; Wittmann et al. 2015). Three EMP analyses display Ni- versus Co-positive correlation that may track direct contamination from chondrite-derived Fe-Ni metals (Ni/Co = 10–20; Fig. 10). Despite careful scans of six BSE maps at high magnification, no other impactor-derived Ni-Fe metal particles have been detected in NWA 7533, neither in pyrite, nor in other lithologies. Such metals are not expected to survive the strongly oxidizing felsic magmas involved in the breccias (Humayun et al. 2014) and subsequent water-rich Martian alteration that produced hydroxylated Fe oxides from the nominally anhydrous Fe (Ti) oxides (Beck et al. 2015; Muttik et al. 2014a, 2014b). Replacement microtextural relationships between oxides and pyrite suggests that meteoritic metal was likely oxidized into Fe (Ti) oxides well before pyrite formation, then those oxides served as the Fe-Ni-Co reservoir for pyrite, perhaps several billion years later.

Like pyrite, platinum-group minerals are very scarce in Martian meteorites. The only known occurrences are two Os-Ir alloy microparticles exsolved from Fe sulfides in the highly shocked chassignite NWA 2737 (Lorand et al. 2012). The two refractory PGE-rich particles analyzed in NWA 7533 cannot be interpreted this way as one grain is included in apatite. Both show some similarities to chondritic refractory metal nuggets identified in carbonaceous chondrites (CM, CV; e.g., Hewins et al. 2014c) in terms of grain size and Os-Ir rich compositions. They could be impactor debris of carbonaceous chondrite impactors identified from bulk-rock highly siderophile element (HSE) analyses on NWA 7034 (Goderis et al. 2014). HSE are by far more resistant to oxidation compared to Ni and Co (Arculus and Delano 1981). However, their association with S and As, two diagnostic elements for hydrothermal fluids suggests that part of these (chondritic?) HSE microparticles were processed by sulfurization reactions with the fluid that precipitated pyrite.

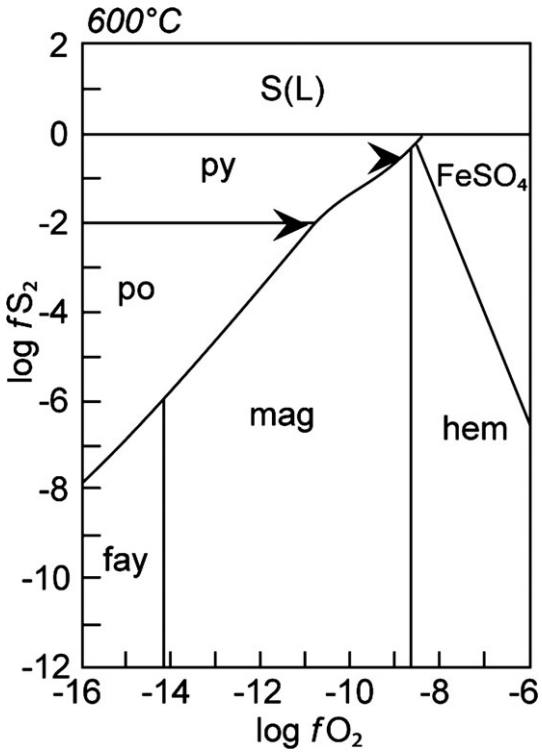

Fig. 13. Log fS_2 versus log fO_2 diagram for the Fe-S-O system at 600 °C (Parat et al. 2011). Arrows delineate the range of redox conditions inferred for NWA 7533. Hem = hematite.

Pyrite Growth Processes in Regolith Breccias

Pyrite is well known to possess a very sluggish nucleation rate and relatively fast crystal growth rate (Rickard and Luther [2007] and references therein). Thus, direct nucleation from solution is unlikely. Most pyrite-producing reaction pathways involve precursor FeS reacting either with H_2S in acidic and oxidizing

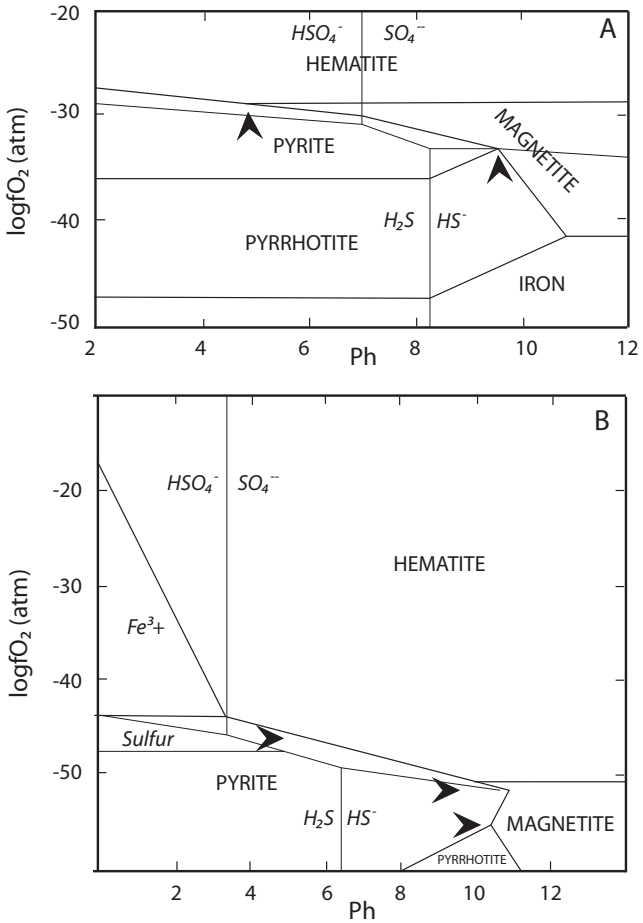

Fig. 14. Log fO_2 versus Ph diagrams for the Fe-S-O system at T = 300 °C (A; Vaughan and Craig 1978), and 125 °C (B; Wang et al. 2010). Arrows delineate the range of redox conditions inferred for NWA 7533.

conditions (as in terrestrial ocean hydrothermal sulfides) or with polysulfide species (S_n^{2-}) in alkaline conditions (Rickard 1997; Ohfuji and Rickard 2005; Gartman and Luther 2013). The FeS surface provides the active sites necessary to overcome the nucleation energy barrier. The FeS precursor is a viable mechanism for vein-filling pyrite that is remote from any available Fe sink. There is also ample evidence that NWA 7533 pyrite either used the iron available from pyroxenes (both low-Ca and high-Ca pyroxene) or nucleated on (and from) Fe-Ti oxides. Pyrite can also form when magnetite reacts with H_2S-rich fluids in oxidizing conditions (plausible for NWA 7533), in line with the reaction below

$$Fe_3O_4 + 6H_2S + O_2 = 3FeS_2 + 6H_2O$$

(Qian et al. 2010).

Micron-sized highly fractured iron oxides in NWA 7533 provided highly active surfaces catalyzing this sulfidation process (Rickard 1997). The morphology and size of pyrite crystals are good indicators of degree of supersaturation and growth rate. Extreme growth rates (and largest degrees of oversaturation) yield submicron-sized raspberry-textured ("framboid") pyrite. Such textures have not been observed in NWA 7533, nor is there evidence of multistage growths marked by framboidal cores and euhedral rims (e.g., McClay and Ellis 1983; Velasquez et al. 2014). Cubes have the lowest Gibbs free energy of formation and their {100} faces the lowest atom density and the highest growth rate, which makes cubic crystals and cubo-octahedra form spontaneously from H_2S fluids, without requiring a high degree of supersaturation (Wang et al. 2010; Barnard and Russo 2007). Octahedral {111} faces have higher atom density, and slower growth rates. Clearly, the size and shape of NWA 7533 pyrite crystals argue for growth from just-saturated H_2S-HS^-(S_n^{2-}) sulfurous fluids with moderate to slow growth rate consistent with a reheating event affecting regolith breccias. Other experimental studies on pyrite point to an effect of pH on pyrite morphologies (Wang et al. 2010; Gartman and Luther 2013). Octahedral pyrite preferentially precipitates from polysulfide species (S_n^{2-}) in mildly alkaline conditions.

Pyrite and the Martian Chronology of NWA 7533

Pyrite is a late mineral, perhaps one of the latest in the Martian chronology of NWA 7533, as it may obstruct fracture planes cutting across all of some thin sections while occurring as disseminated crystals inside all of the lithologies (clasts, lithic clasts, CLIMR, ICM melt spherules). In more detail, ICM may contain both highly denticulated pyrite aggregates that enclose abundant matrix mineral inclusions and euhedral pyrite which grew freely in a semiconsolidated medium, without trapping abundant surrounding minerals. The only interpretation that may reconcile all these contradictory observations is that pyrite crystallized from repeated pulses of S-rich hydrothermal fluids after the final assembly of the breccia and during lithification and compaction that made it cohesive. Final pulses occurred when the breccia behaved brittlely, thus generating the pyrite-filled vein systems by hydraulic fracturing. It has been shown above that pyrite started crystallizing at high (~400–500 °C) temperature, starting from the most Ni-rich crystals and continuing down temperature to pure pyrite. Latent heat release by pyrite crystallization may have helped lithification of surrounding minerals on a local scale and development of an Fe-depleted inner zone inside radiating pyroxene coronas. There is also good reason for relating that pyrite formation event to the short-duration, thermal event that produced the granoblastic microstructure of fine-grained matrix crystals (Muttik et al. 2014a, 2014b).

Several radiogenic isotope systematics provide a late (around 1.4 Ga) age for such a thermal event. The alkali-feldspars in leucocratic clasts record a very short-lived resetting event or mixing between feldspars and the whole rock at 1.4 Ga (Bellucci et al. 2015). Ages at 1.4 Ga were recently identified in the Re-Os systematics of bulk sample fractions of NWA 7034 (Goderis et al. 2014). This widespread thermal metamorphic event postdating the final assembly of the breccia is supported by Ar-Ar ages on feldspars (Lindsay et al. 2014) and similar Pb-Pb age resetting at 1.36–1.45 Ga in phosphates from all matrix domains of NWA 7034 and NWA 7533 (Bellucci et al. 2015). The closure temperature for apatite Pb diffusion is 450–500 °C (Cherniak et al. 1991), which means that about 1.4 Ga ago, the temperature conditions were suitable for pyrite formation in NWA 7533.

Regarding the origin of sulfur, only a multi-isotope S study could help in discriminating magmatic (i.e., leached from underlying basaltic intrusions or degassed from volcanism) from recycled surface sulfur (sulfates) (Farquhar et al. 2007; Franz et al. 2014). The Noachian regolith breccias NWA 7533 and paired stones provide evidence for massive and pervasive growth of large pyrite crystals, which supports a regional scale event that released S-rich hydrothermal waters. Impact(s) at ~1.4 Ga may be good candidate(s) for triggering this hydrothermal activity. Formation of pyrite in this way was suggested for the Meridiani Planum depression (Zolotov and Shock 2005) and the Noachian Gale crater (Schwenzer et al. 2012). It is well known that impacts can trigger hydrothermal convection returning surface fluids and solid components into deeper seated crustal rocks (Naumov 2002) while they may release S-rich volatile-rich hydrothermal fluids (Newsom et al. 1999; Schwenzer et al. 2012). It has been suggested above that NWA 7533 pyrite formed from saturated solutions with moderate growth rate consistent with a strongly reheated host rock. Cooling rates in impact structures are high enough in the uppermost melt-rich part (10^7 °C Ma^{-1}) and much lower in the deeper portion of the impact structure. Hence, the most intense hydrothermal activity in impact craters develops within this lower, more slowly cooled portions (e.g., Naumov 2002; Squyres et al. 2012).

CONCLUSION

Martian regolith meteoritic breccias NWA 7533 and paired stones put forward strong evidence that the S budget of the earliest Noachian crust was deeply rejuvenated by much later hydrothermal events coeval with late impactors and short-duration annealing of the meteorite.

Pyrite precipitated from hot, hydrothermal H_2S-HS^-(S_n^{2-}) sulfurous fluids percolating the strongly oxidized, magnetite–maghemite-bearing regolith breccias. Pyrite is more oxidized and more stable than pyrrhotite in this context. Pyrite likely incorporated a lot of strongly modified chondritic impactor debris such as Ni, Fe, Co and some highly siderophile elements, depending on the availability of that debris in the vicinity of pyrite nuclei. However, because of redox conditions, siderophiles were first incorporated in silicates and Fe (Ti) oxide structures and were later transferred to pyrites by sulfurization reactions that took place perhaps a couple of billion years later. Then Ni stabilized pyrite at high temperatures on Mars while limiting its alteration on Earth.

Highly acidic weathering models that were suggested for explaining Martian sulfate deposits may be inefficient for the southern hemisphere Noachian crust, owing to the lack of pyrrhotite as bedrock sulfides. Because it is more oxidized, pyrite is 20 times less reactive than pyrrhotite which contains metal defects that serve as nucleation centers for oxidation (Belzille et al. [1997] and references therein). One may speculate that pyrite crystals remained mostly unfractured on Mars and thus much less prone to oxy-hydration until the shock event that liberated the meteorite from Mars.

Although very scarce, the few Ni pyrrhotite + pentlandite microinclusions observed in plagioclase and K-feldspar clasts track an earlier generation of magmatic sulfides akin to those reported in SNC meteorites. One may speculate that this magmatic sulfide generation was preserved exceptionally inside feldspar clasts. The rest was either totally volatilized by repeated impacts affecting regolith breccias, or dissolved during subsequent hydrous alteration events.

Acknowledgments—Financial funding was provided by a INSU 2014-PNP grant (JPL, RH, BZ, SP), and by the NASA Cosmochemistry program (MH). The National NanoSIMS facility at the MNHN was established by funds from the CNRS, Région Ile de France, Ministère délégué à l'Enseignement supérieur et à la Recherche, and the MNHN. The authors thank Michel Fialin (Camparis) for his help with electron microprobe analyses. They thank David Troadec (IEMN, University of Lille) for the preparation of the FIB-TEM sample. The TEM national facility in Lille (France) is supported by the Conseil Regional du Nord-Pas de Calais, the European Regional Development Fund (ERDF) and the Institut National des Sciences de l'Univers (INSU, CNRS). We thank C. Ferraris and G. Carlier for providing standards of oxyhydroxide from the mineral collection of the Museum National d'Histoire Naturelle.

The final version of the paper was greatly improved thanks to comments from an anonymous reviewer and editorial supervision by Ed Scott.

Editorial Handling—Dr. Edward Scott

REFERENCES

Agee C. B., Wilson N. V., Mc Cubbin F. M., Ziegler K., Polyak V. J., Sharp Z. D., Asmerom Y., Nunn M. H., Shaheen R., Thiemens M. H., Steele A., Fogel M. L., Bowden R., Glamoclija M., Zhang Z., and Elardo S. E. 2013. Unique meteorite from Early Amazonian Mars: Water-rich basaltic Breccia Northwest Africa7034. *Science* 339:780–785.

Arculus R. and Delano J. 1981. Siderophile element abundances in the upper mantle: Evidence for a sulfide signature and equilibrium with the core. *Geochimica et Cosmochimica Acta* 45:1331–1343.

Barnard A. S. and Russo S. P. 2007. Shape and thermodynamic stability of pyrite FeS_2 nanocrystals and nanorods. *Journal of Physics and Chemistry* 111:11,742–11,746.

Beck P., Pommerol A., Remusat L., Zanda B., Lorand J.-P., Göpel C., Hewins R. H., Pont S., Lewin E., Quirico E., Schmitt B., Montes-Hernandez G., Garenne A., Bonal L., Proux O., Hazemann J. L., and Chevrier V. C. F. 2015. A Noachian source region for the "Black Beauty" meteorite, and a source lithology for Mars surface hydrated dust? *Earth and Planetary Science Letters* 427:104–111.

Bellucci J. J., Nemchin A. A., Whitehouse M. J., Humayun M., Hewins R., and Zanda B. 2015. Pb-isotopic evidence for an early, enriched crust on Mars. *Earth and Planetary Science Letters* 410:34–41.

Belzille N., Maki S., Chen Y.-W., and Goldsack D. 1997. Inhibition of pyrite oxidation by surface treatment. *Science of the Total Environment* 196:177–186.

Bridges J. C. C., Catling D. C., Saxton J. M., Lyon I. C., and Grady M. M. 2001. Alteration assemblages in Martian meteorites: Implications for near-surface processes. *Space Science Review* 96:365–392.

Burns R. G. and Fisher D. S. 1990. Iron-sulfur mineralogy of Mars: Magmatic evolution and chemical weathering products. *Journal of Geophysical Research* 95(B9):14,415–14,421.

Cherniak D. J., Lanford W. A., and Ryerson F. J. 1991. Lead diffusion in apatite and zircon using ion implantation and Rutherford backscattering techniques. *Geochimica et Cosmochimica Acta* 55:1663–1673.

Chevrier V., Rochette P., Mathe P. E., and Grauby O. 2004. Weathering of iron-rich phases in simulated Martian atmospheres. *Geology* 32:1033–1036.

Chevrier V., Roy R., Le Mouélic S., Borschneckc D., Mathe P. E., and Rochette P. 2006. Spectral characterization of weathering products of elemental iron in a Martian atmosphere: Implications for Mars hyperspectral studies. *Planetary and Space Sciences* 54:1034–1045.

Chevrier V., Lorand J.-P., and Sautter V. 2011. Sulfide petrology of four nakhlites (NWA817, NWA998, Nakhla, Governador Valadares). *Meteoritics & Planetary Science* 46:769–784.

Cornell R. M. and Schwertmann U. 1996. *The iron oxides: Structure, properties, reactions, occurrence, and uses*, vol. 1. Weinheim, Germany: VCH. 573 p.

Craig J. R. and Vokes F. M. 1993. The metamorphism of pyrite and pyritic ores: An overview. *Mineralogical Magazine* 57:3–18.

Cudennec Y. and Lecerf A. 2006. The transformation of ferrihydrite into goethite or hematite, revisited. *Journal of Solid State Chemistry* 179:716–722.

Dehouck E., Chevrier V., Gaudin A., Mangold N., Mathe P. E., and Rochette P. 2012. Evaluating the role of sulfide-weathering in the formation of sulfates or carbonates on Mars. *Geochimica et Cosmochimica Acta* 90:47–63.

Dreibus G., Palme H., Spettel B., Zipfel J., and Wanke H. 1995. Sulfur and selenium in chondritic meteorites. *Meteoritics* 30:439–445.

Durocher J. L. and Schindler M. 2011. Iron-hydroxide, iron-sulfate and hydrous-silica coatings in acid-mine tailings facilities: A comparative study of their trace-element composition. *Applied Geochemistry* 26:1337–1352.

Dyar M. D., Tucker J. M., Humphries S., Clegg S. M., Wiens R. C., and Lan M. D. 2011. Strategies for Mars remote laser-induced breakdown spectroscopy analysis of sulfur in geological samples. *Spectrochimica Acta* 66:39–56.

Farquhar J., Kim S. T., and Masterson A. 2007. Implications from sulfur isotopes of the Nakhla meteorite for the origin of sulfate on Mars. *Earth and Planetary Science Letters* 264:1–8.

Fernandez-Remolar D., Gomez-Elvira J., Gomez F., Sebastian E., Martiin J., Manfredi J. A., Torres J., Gonzalez Kesler C., and Amils R. 2004. The Tinto River, an extreme acidic environment under control of iron, as an analog of the Terra Meridiani hematite site of Mars. *Planetary Space Science* 52:239–248.

Floran R. J., Prinz M., Hlava P. F., Keil K., Nehru C. E., and Hinthorne J. R. 1978. The Chassigny meteorite: A cumulate dunite with hydrous amphibole-bearing melt inclusions. *Chemical Geology* 42:1213–1222.

Franz H. H., Kim S. T., Farquhar J., Day J. M. D., Economos R. C., McKeegan K., Schmit A. K., Irving A. J., Hoek J., and Dottin J. III. 2014. Isotopic links between atmospheric chemistry and the deep sulfur cycle on Mars. *Nature* 508:365–368.

French B. M. 1998. A handbook of shock-metamorphic effects in terrestrial meteorite impact structures. Shock-metamorphic effects in rocks and minerals traces of catastrophe. LPI Contribution 954. Houston, Texas: Lunar and Planetary Institute. 120 p.

Gartman A. and Luther G. W. 2013. Comparison of pyrite (FeS_2) synthesis mechanisms to reproduce natural FeS_2 nanoparticles found at hydrothermal sites. *Chemical Geology* 120:447–458.

Gattacceca J., Hewins R. J., Lorand J.-P., Rochette P., Lagroix F., Cournède C., Uehara M., Pont S., Sautter V., Scorzelli R. B., Hombourger C., Munayco P., Zanda B., and Chennaoui H. 2013. Opaque minerals, magnetic properties and paleomagnetism of the Tissint Martian meteorite. *Meteoritics & Planetary Science* 48:1919–1936.

Gattacceca J., Rochette P., Scorzelli R. B., Munayco P., Agee C., Quesnel Y., Cournède C., and Geissman J. 2014. Martian meteorites and Martian magnetic anomalies: A new perspective from NWA 7034. *Geophysical Research Letters* 41, doi:10.1002/2014GL060464.

Gendrin R. A., Mangold N., Bibring J. P., Langevin Y., Gondet B., Poulet F., Bonello G., Quantin C., Morris R. V., Mustard J. F., Arvidson R. E., and LeMouélic S. 2005. Sulfates in Martian layered terrains: The OMEGA/Mars Express view. *Science* 307:1587–1591.

Goderis S., Brandon A. D., Mayer B., Humayun M., and Agee C. B. 2014. Tracing impactor signals prevalent in Martian regolith breccia Northwest Africa 7034 with Os isotopes and platinum group elements (abstract #2200). 45th Lunar and Planetary Conference. CD-ROM.

Greenwood J. P., Mojzsis S. J., and Coath C. D. 2000. Sulfur isotopic compositions of individual sulfides in Martian meteorites ALH 84001 and Nakhla: Implications for crust-regolith exchange on Mars. *Earth and Planetary Science Letters* 184:23–34.

Greenwood J. P., Itoh S., Sakamoto N., Vicenzi E. P., and Yurimoto H. 2008. Hydrogen isotope evidence for loss of water from Mars through time. *Geophysical Research Letters* 35:L05203.

Hannington M. A., Galley A. D., Herzig PM, and Petersen S. 1998. Comparison of the TAG mound and stockwork complex with Cyprus-type massive sulfides. In *Proceedings ODP: Scientific Results, 158*, edited by Herzig P. M., Humphris S. E., Miller D. J., and Zierenberg R. A. (College Station, Texas: Ocean Drilling Program.) pp. 389–415.

Herd C. D. K., Borg L. E., Jones J. H., and Papike J. J. 2002. Oxygen fugacities and geochemical variations in the Martian basalts: Implications for Martian basalt petrogenesis and the oxidation state of the upper mantle of Mars. *Geochimica et Cosmochimica Acta* 66:2025–2036.

Herzig P. M. and Hannington M. D. 1995. Polymetallic massive sulfides at the modern seafloor: A review. *Ore Geology Review* 10:95–115.

Hewins R. H., Zanda B., Humayun M., Lorand J.-P., Deldicque D., Pont S., Fieni C., Nemchin A., Grange M., Kennedy A., Göpel C., and Lewin E. 2013. Petrology of NWA 7533, formation by impact of old Martian crust (abstract #5252). *Meteoritics & Planetary Science* 48.

Hewins R. H., Zanda B., Humayun M., Lorand J.-P., and Pont S. 2014a. Impact melt rocks and pristine clasts in Martian breccia NWA 7533 (abstract #1416). 45th Lunar and Planetary Science Conference. CD-ROM.

Hewins R. H. and NWA 7533 Consortium. 2014b. Ancient meteorite breccias from Mars (abstract #5338). *Meteoritics & Planetary Science* 49.

Hewins R. J., Bourot-Denise M., Zanda B., Leroux H., Barrat J.-A., Humayun M., Göpel C., Greenwood R. C., Franchi I. A., Pont S., Lorand J.-P., Cournède C., Gattaceca J., Rochette P., Kuga M., Marrochi Y., and Marty B. 2014c. The Paris meteorite, the less altered CM chondrite so far. *Geochimica et Cosmochimica Acta* 124:190–222.

Humayun M., Nemchin A. A., Zanda B., Hewins R. H., Grange M., Kennedy M., Lorand J.-P., Göpel C., Pont S., Fieni C., and Deldicque D. 2013. Origin and age of the earliest Martian crust from meteorite 7533. *Nature* 503:513–516.

Humayun M., Hewins R. H., Lorand J.-P., and Zanda B. 2014. Weathering and impact melting determined the mineralogy of the early Martian crust preserved in Northwest Africa 7533 (abstract #1880). 45th Lunar and Planetary Conference. CD-ROM.

Huminicki D. M. C. and Rimstidt J. D. 2009. Iron oxyhydroxide coating of pyrite for acid mine drainage control. *Applied Geochemistry* 24:1626–1634.

Hurowitz J. A., McLennan S. M., Tosca N. J., Arvidson R. E., Michalski J. P., Ming D. W., Schröder C., and Squyres S. W. 2006. In situ and experimental evidence for acidic weathering of rocks and soils on Mars. *Journal of Geophysical Research* 111:EO2S19.

Hurowitz J. A., Fisher W., Tosca N. J. and Milliken R. E. 2010. Origin of acidic surface waters and the evolution of atmospheric chemistry on early Mars. *Nature Geoscience* 3:323–326.

Huston D. L., Sie S. H., Suter G. F., Cooke D. R., and Both R. A. 1995. Trace elements in sulfide minerals from eastern Australian volcanic-hosted massive sulfide deposits: Part I. Proton microprobe analyzes of pyrite, chalcopyrite, and sphalerite, and part II. Selenium levels in pyrite: Comparison with $\delta^{34}S$ values and implications for the source of sulfur in volcanogenic hydrothermal systems. *Economic Geology* 90:1167–1190.

Jerz J. K. and Rimstidt J. D. 2004. Pyrite oxidation in moist air. *Chemical Geology* 68:701–714.

King P. L. and McLennan S. M. 2010. Sulfur on Mars. *Elements* 6:107–112.

Klingelhöffer G., Morris R. V., Bernhardt B., Schroder C., Rodionov D. S., De Souza P. A., Yen A. S., Gellert R., Evlanov E. N., Zubkhov V., Foh J., Bonnes U., Kankeleit E., Gutlich P., Ming D. W., Renz F., Wdowiak R., Squyres S. W., and Arvidson R. E. 2004. Jarosite and hematite at Meridiani Planum from Opportunity's Mössbauer spectrometer. *Science* 306:1740–1745.

Knauth L. P., Burt D. M., and Wohletz K. 2005. Impact origin of sediments at the Opportunity landing site on Mars. *Nature* 438:1123–1128.

Lee M. R. and Bland P. A. 2004. Mechanisms of weathering of meteorites recovered from hot and cold deserts and the formation of phyllosilicates. *Geochimica et Cosmochimica Acta* 68:893–916.

Lindsay F. N., Turrin B. D., Göpel C., Herzog G. F., Zanda B., Hewins R., Park J., Delaney J. S., and Swisher C. C. 2014. $^{40}Ar/^{39}Ar$ ages of Martian meteorite NWA 7533 (abstract #5383). Meteoritics & Planetary Science 49.

Lorand J.-P. and Alard O. 2011. Pyrite tracks assimilation of crustal sulfur in some Pyrenean lherzolites. *Mineralogy and Petrology* 101:115–128.

Lorand J.-P., Chevrier V., and Sautter V. 2005. Sulfide mineralogy and redox conditions in some Shergottites. *Meteoritics & Planetary Science* 40:1257–1272.

Lorand J.-P., Alard O., and Luguet A. 2010. Platinum-group element micronuggets and refertilization process in the Lherz peridotite. *Earth and Planetary Science Letters* 289:298–310.

Lorand J.-P., Barrat J.-A., Chevrier V. C. F., Sautter V., and Pont S. 2012. Metal-saturated sulfide assemblages in chassignite NWA 2737; evidence for impact-related sulfur devolatilisation. *Meteoritics & Planetary Science* 47:1830–1841.

Lorand J.-P., Hewins R. H., Remusat L., Zanda B., Humayun M., Nemchin A., Grange M., Kennedy M., Göpel C., and Pont S. 2014. Pyrite tracks late hydrothermal alteration in Martian regolith breccia NWA 7533 (abstract). *Meteoritics & Planetary Science* 49:A241.

Luguet A., Lorand J.-P., Alard O., and Cottin J. Y. 2004. A multi-technique study of platinum-group elements systematic in some Ligurian ophiolitic peridotites, Italy. *Chemical Geology* 208:175–194.

McClay K. R. and Ellis P. G. 1983. Deformation and recrystallization of pyrite. *Mineralogical Magazine* 47:527–538.

McCollom T. M. and Hynek B. M. 2005. A volcanic environment for bedrock diagenesis at Meridiani Planum on Mars. *Nature* 438:1129–1132.

Moncur M. C., Jambor J., Ptacek K., and Blowes D. H. 2009. Mine drainage from the weathering of sulfide minerals and magnetite. *Applied Geochemistry* 24:2362–2373.

Muttik N., Agee C. B., McCubbin F. M., McHutcheon W. A., Provencio P. P., Keller L. P., Santos A. R., and Chearer C. K. 2014a. Looking for a sourcer of water in Martian basaltic breccia NWA 7034 (abstract #2783). 45th Lunar and Planetary Science Conference. CD-ROM.

Muttik N., McCubbin F. M., Keller L. P., Santos A. S., McCutcheon M. C., Provencio P. P., Rahman Z., Shearer C. K., Boyce J. W., and Agee C. B. 2014b. Inventory of H_2O in the ancient Martian regolith from Northwest Africa 7034: The important role of Fe oxides. *Geophysical Research Letters* 41:2014G. doi:10.1002/L062533.

Naumov M. V. 2002. Impact-generated hydrothermal systems: Data from Popigai, Kara, and Puchezh-Katunki impact structures. In *Impacts in Precambrian shields*, edited by Plado J. and Pesonen L. J. Berlin: Springer. pp 117–171.

Nemchin A., Humayun M., Whitehouse M. J., Hewins R. H., Lorand J.-P., Kennedy M., Grange M., Zanda B., Pont S., and Deldicque D. 2014. Record of ancient Martian hydrosphere preserved in zircon from NWA 7533. *Nature Geosciences* 7:638–642.

Nesbitt H. W., Bancroft G. M., Pratt A. R., and Scaini M. J. 1998. Sulfur and iron surface states on fractured pyrite surfaces. *American Mineralogist* 83:1067–1076.

Newsom H. E., Haggerty J. J., and Goff F. 1999. Mixed hydrothermal fluids and the origin of the Martian soil. *Journal of Geophysical Research* 104(E4):8717–8728.

Ohfuji H. and Rickard D. 2005. Experimental syntheses of framboids—A review. *Earth Science Reviews* 71:147–170.

Papike J. J., Karner J. M., Shearer C. M., and Burger P. V. 2009. Silicate mineralogy of Martian meteorites. *Geochimica et Cosmochimica Acta* 73:7443–7485.

Parat F., Holz F., and Streck M. J. 2011. Sulfur-bearing magmatic accessory minerals. *Reviews in Mineralogy and Geochemistry* 73:285–331.

Pratt A. R., Nesbitt H. W., and Mycroft J. R. 1996. The increased reactivity of pyrrhotite and magnetite phases in sulfide mine tailings. *Journal of Geochemical Exploration* 56:I–II.

Qian G., Brugger J., Skinner W. L., Chen G., and Pring A. 2010. An experimental study of the mechanism of the replacement of magnetite by pyrite up to 300 °C. *Chemical Geology* 74:5610–5630.

Rickard D. 1997. Kinetics of pyrite formation by the H_2S oxidation of iron (II) monosulfide in aqueous solutions between 25 and 125°C: The rate equation. *Chemical Geology* 61:115–134.

Rickard D. and Luther G. W. 2007. Chemistry of iron sulfides. *Chemical Review* 107:514–56.

Rochette P., Lorand J.-P., Fillion G., and Sautter V. 2001. Remanent magnetization of basaltic shergottites carried by pyrrhotite: A changing perspective on Martian magnetism. *Earth and Planetary Science Letters* 190:1–12.

Schwenzer S. P., Abramov Allen C. C., Bridges J., Clifford S. M., Filiberto J., Kring D. A., Lasue J., McGovern P. J., Newsom H. E., Treiman A. H., Vaniman D. T., Wiens R. C., and Wittmann A. 2012. Gale crater: Formation and post-impact hydrous environments. *Planetary and Space Science* 70:84–95.

Scott E. R. D. 1999. Origin of carbonate-magnetite-sulfide assemblages in Martian meteorite ALH 84001. *Journal of Geophysical Research* 104:3803–3813.

Shearer C. K., Layne G. D., Papike J. J., and Spilde M. N. 1996. Sulfur isotopic systematics in alteration assemblages in Martian meteorite ALH 84001. *Chemical Geology* 60:2921–2926.

Song Y., Swedlund P. J., Zou C., and Hamid R. D. 2013. The influence of surface structure on H_4SiO_4 sorption and oligomerization on goethite surfaces: An XPS study using goethites differing in morphology. *Chemical Geology* 347:114–122.

Squyres S. W., Arvidson R. E., Bell J. F., Calef F., Clark B. C., Crumpler L. A., De Souza P. A., Farrand W. H., Gellert R., Grant J. A., Herkenhoff K. E., Hurowitz J. A., Johnson J. R., Jolliff B. L., Knoll A. H., Li R., McLennan S. M., Ming D. W., Mittlefehldt D. W., Parker T. J., Paulsen G., Rice M. S., Ruff S. W., Schröder C., Yen A. S. and Zacny K. 2012. Ancient impact and aqueous processed at Endeavour crater, Mars. *Science* 376:570–576.

Stephant L., Remusat A., Thomen F., and Robert F. 2014. Reduction of OH contamination in quantification of water contents using NanoSIMS imaging. *Chemical Geology* 380:20–26.

Stöffler D. and Grieve R. A. F. 2007. Impactites. In *Metamorphic rocks: A classification and glossary of terms, recommendations of the international union of geological sciences*, edited by Fettes D. and Desmons J. Cambridge, UK: Cambridge University Press. pp. 82–92, 111–125, and 126–246.

Tosca N. J., Lennan S. M., Lindsley D., and Schoonen M. A. A. 2004. Acid-sulfate weathering of synthetic Martian basalt: The acid fog model revisited. *Journal of Geophysical Research—Planets* 109:EO5003.

Tuff J., Wade J., and Wood B. J. 2013. Volcanism on Mars controlled by early oxidation of the upper mantle. *Nature* 498:342–345.

Vaniman D. T., Bish D. L., Ming D. W., Bristow T. F., Morris R. V., Blake D. F., Chipera S. J., Morrison S. M., Treiman A. H., Rampe E. B., Rice M., Achilles C. N., Grotzinger J. P., McLennan S. M., Williams J., Bell J. F. III, Newsom H. E., Downs R. T., Maurice S., Sarrazin P., Yen A. S., Morookian J. M., Farmer J. D., Stack K., Milliken R. E., Ehlmann B. L., Sumner D. Y., Berger G., Crisp J. A., Hurowitz J. A., Anderson R., Des Marais D. J., Stolper E. M., Edgett K. S., Gupta S., and Spanovich N. 2013. Mineralogy of a mudstone at Yellowknife Bay, Gale crater, Mars. *Science* 343:1243480. doi:10.1126/science.1243480.

Vaughan D. J. and Craig J. R. 1978. Mineral chemistry of metal sulfides. *Earth science series*, edited by Harland W. B., Cook A. H., and Hughes N. F. Cambridge: Cambridge University Press. 493 p.

Velasquez G., Béziat D., Salvi S., Siebenaller L., Borisova A. Y., Pokrovski G. S., and de Parseval P. 2014. Formation and deformation of pyrite and implications for gold mineralization in the El Callao District, Venezuela. *Economic Geology* 109:457–486.

Wang D., Wang Q., Wang T., and MSL Science Team. 2010. Shape controlled growth of pyrite FeS_2 crystallites via a polymer- assisted hydrothermal route. *Crystal Engineering Communication* 12:3797–3805.

Webster C. R., Mahaffy P. R., Flesch G. J., Niles P. B., Jones J. H., Leshin L. A., Atreya S. K., Stern J. C., Christensen L. E., Owen T., Franz H., Pepin R. O., and Steele A., and the MSL Science Team. 2013. Isotope ratios of H, C, and

O in CO_2 and H_2O of the Martian atmosphere. *Science* 341:260–263.

Wittmann A., Korotev R. L., Jolliff B. L., Irving A. J., Moser D. E., Barker I., and Rumble D. G. III. 2015. Petrography and composition of Martian regolith breccia meteorite Northwest Africa 7455. *Meteoritics & Planetary Science* 50:326–352.

Yamaguchi A., Scott E. R. D., and Keil K. 1999. Origin of a unique impact melt-rock: The L-chondrite Ramsdorf. *Meteoritics & Planetary Science* 34:49–59.

Zolotov M. Y. and Shock E. L. 2005. Formation of jarosite-bearing deposits through aqueous oxidation of pyrite at Meridiani Planum, Mars. *Geophysical Research Letters* 32: L21203.